ktu
1922

Kaunas University of Technology

Faculty of Mathematics and Natural Sciences

A method for the quantitative discrimination of breast tissue chemical composition based on the spectral decomposition of X-ray tomographic breast images

Master's Final Degree Project

Stevan Vrbaški

Project author

Prof. Diana Adliene
Prof. Renata Longo
Ph.D. Adriano Contillo

Supervisor

Kaunas, 2020

Kaunas University of Technology

Faculty of Mathematics and Natural Sciences

A method for the quantitative discrimination of breast tissue chemical composition based on the spectral decomposition of X-ray tomographic breast images

Master's Final Degree Project

Medical Physics (6213GX001)
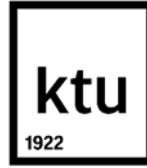
Stevan Vrbaški

Project author

Prof. Diana Adliene
Prof. Renata Longo
Ph.D. Adriano Contillo

Supervisors

Mantas Sriubas

Reviewer

Kaunas, 2020

Kaunas University of Technology

Faculty of Mathematics and Natural Sciences

Stevan Vrbaški

A method for the quantitative discrimination of breast tissue chemical composition based on the spectral decomposition of X-ray tomographic breast images

Declaration of Academic Integrity

I confirm that the final project of mine, Stevan Vrbaški, on the topic "A method for the quantitative discrimination of breast tissue chemical composition based on the spectral decomposition of X-ray tomographic breast images" is written completely by myself; all the provided data and research results are correct and have been obtained honestly. None of the parts of this thesis have been plagiarised from any printed, Internet-based or otherwise recorded sources. All direct and indirect quotations from external resources are indicated in the list of references. No monetary funds (unless required by Law) have been paid to anyone for any contribution to this project.

I fully and completely understand that any discovery of any manifestations/case/facts of dishonesty inevitably results in me incurring a penalty according to the procedure(s) effective at Kaunas University of Technology.

Stevan Vrbaški
(name and surname filled in by hand)

(signature)

Summary

Breast cancer is one of the leading causes of death for women worldwide. Early and accurate detection of malignancies is essential for improving the outcome of cancer treatments. Conventional X-ray imaging is based purely on contrasts of attenuation and, since no contrast difference between cancerous and glandular tissues is evident, the diagnosis is mainly based on the morphological characteristics of cancer. On the other hand, advanced imaging techniques allow the extraction of quantitative information. We aim to exploit a technique of spectral decomposition to quantify the difference in chemical composition between healthy and malignant dense tissues. The study was carried out using a custom-made phantom, filled with water and containing inserts of plastic materials (polyethylene, nylon, polymethyl methacrylate, polyoxymethylene, polytetrafluoroethylene) that mimic the attenuation properties of breast tissues. Imaging was performed at Elettra, the Italian synchrotron facility, using monochromatic beams of several energies in the breast CT imaging energy range (25-35 keV). 3D tomographic maps of attenuation coefficients were obtained by acquiring projections in a free space propagation phase-contrast setup and further processing them utilizing a phase retrieval filter, a procedure resulting in a significant noise reduction without loss of spatial resolution. Images were processed by a spectral decomposition algorithm, resulting in composition maps in terms of a selected pair of basis materials. Material choice matched the tissue range of interest inside the breast. Using a dedicated mathematical procedure, we managed to decouple the information about the material density and its chemical composition. Finally, a calibration allowed for the extraction of the effective atomic number associated to each reconstructed voxel. The range of effective atomic numbers among the plastic inserts matched the slight differences among tissues in the breast. Compared to previous studies, the present approach exhibits a much higher sensitivity in material discrimination, which is necessary for the context of breast diagnostic imaging. The decoupling of the information about the chemical composition allows very accurate discrimination of similar tissues composing the breast. The proposed technique of spectral decomposition and decoupling allows a quantitative description of imaged samples composition, opening the possibility of significant contributions to a breast cancer diagnosis.

Vrbaški Stevanas. Kokybinis krūties audinio cheminės sudėties nusta tymo metodas paremtas spektrine kompiuterinės tomografijos vaizdų analize. Magistro baigiamojo laipsnio projektas / prof. Diana Adlienė, prof. Renata Longo, Ph.D. Adriano Contillo; Kauno technologijos universiteto Matematikos ir gamtos mokslų fakultetas.

Studijų sritis ir sritis (studijų srities grupė): Sveikatos mokslai, medicinos technologijos (G09)

Raktažodžiai: sinchrotrono spinduliuotė, krūties kompiuterinė tomografija, , fazinio kontrasto vaizdinimas, medžiagų skaidymas, kiekybinė diskriminacija.

Kaunas, 2020. 54 p.

Santrauka

Krūties vėžys yra viena iš pagrindinių moterų mirties priežasčių visame pasaulyje. Ankstyvas ir tikslus piktybinių navikų nustatymas yra labai svarbus siekiant pagerinti vėžio gydymo rezultatus. Įprastinis rentgenodiagnostinis vaizdinimas yra siejamas su kontrasto skirtumais dėl skirtingo spinduliuotės silpimo įvairaus tankio medžigose. Tačiau krūties vėžio atveju nėra akivaizdaus kontrasto skirtumo tarp vėžinių darinių ir liaukinio audinio, todėl diagnozė dažniausiai grindžiama morfologinėmis vėžio savybėmis. Kita vertus, pažangūs vaizdinimo metodai leidžia išgauti kiekybinę informaciją. Šiame darbe buvo siekiama įvertinti sveikų audinių ir piktybinių navikų cheminės sudėties skirtumą naudojant spektrinės dekompozicijos techniką. Tyrimas buvo atliktas naudojant individualų vandeniu užpildytą fantomą, su plastikiniais (polietileno, nailono, polimetilmetakrilato, polioksimetileno, politetrafluoretileno) intarpais, kurie imituoja medžiagas atsakingas už spinduliuotės silpimą krūties audiniuose. Tyrimas buvo atliktas Italijoje, Elettra sinchrotrono centre, naudojant monochromatinę (25-35 keV) fotonų spinduliuotę krūtų kompiuterinės tomografijos vaizdų gavimui. Tikslingai parenkant vaizdo erdvines projekcijas fazinio kontrasto taikymo eksperimentinėje geometrijoje ir vaizdus apdorojant, buvo sudaryti trimačiai silpimo koeficientų tomografijos žemėlapiai. Vaizdų apdorojimui naudojant fazės atkūrimo filtrą ir spektrinės dekompozicijos algoritmą, pavyko ženkliai sumažinti vaizdo triukšmų lygį neprarandant erdvinės skyros ir sudaryti dviejų pasirinktų bazinių medžiagų sudėties žemėlapius. Tyrimui buvo pasirinktos medžiagos, reprezentuojančios krūties audinius. Specialaus matematinio algoritmo pagalba pavyko atsieti informaciją apie medžiagos tankį ir jos cheminę sudėtį. Atlikus kalibravimą, tam tikras medžiagos efektyvusis atominis numeris buvo susietas su kiekvienu rekonstruotu vaizdo vokseliu. Į fantomą įterptinių plastikų efektyvieji atominiai numeriai leido formaliai atskirti krūties audinius. Lyginant su ankstesniais tyrimais, darbe siūlomas vaizdinimo metodas leido padidinti panašaus tankio medžiagų diskrimancijos jautrumą, kuris yra ypač svarbus analizuojant krūtų vaizdus. Atsiejus informaciją apie cheminę sudėtį nuo tankio, galima labai tiksliai atskirti panašius audinius, sudarančius krūtį. Siūloma spektrinės dekompozicijos ir parametrų atsiejimo technika leidžia kiekybiškai vertinti krūties diagnostinius vaizdus ir atveria naujas galimybes krūties vėžio diagnostikoje.

List of contents

List of figures

List of tables

Introduction

Breast screening is the most common screening method for the detection of malignancies in women around the world. Many countries developed the strategy of regular mammography examinations in women older than the age of 50 since it has been shown that early diagnoses drastically improve the outcome of cancer treatments. The main reason for such a boundary to be proposed is an outcome of considering the likeliness of tumor development as well as unwanted, but unavoidable, long term radiation risks. According to the International Agency for Research on Cancer (IARC) [1], 20 % of cancer cases were found in women under this age. For younger women, initial ultrasound (US) examinations are instead advised. Breast cancer detection is higher for the woman at the age of 50 to 64, going up to 36% in Europe. American Cancer Society estimated around 300 000 new cases (both sexes) in 2020 in the USA, predicting up to 43 000 deaths [2]. In 2018 in Europe, breast cancer caused around 150 000 death, which indicated the highest mortality among all other cancers. Moving to Asia, statistics changes a bit. Incidence rates are low but increasing more rapidly compared to western countries. Late detection is typical for this part of the world, and the mean age at onset is at a younger age [3]. In general, over 2 million cases in 2018 were reported, representing around 25% of all cancer cases in a woman with an estimated death of half a million around the world, per IACR [1].

Breasts, or mammary glands, are made up of lobules, milk-producing glandular structures, and system of ducts that transport milk. These structures are cumulatively referred to as fibro-glandular tissue. Breasts contain fat and connective tissues as well. Excess fluid is drained by lymphatic vessels. However, almost all carcinomas develop from epithelial cells lining the breast ducts. From the radiological point of view, the critical problem lies in the fact that the tissues comprising the breast are soft tissues of a very similar low atomic number. Developing malignancies share the same property as well. In x-ray radiology, tissues are discriminated based on their linear attenuation coefficients μ. These are dependent on the density and effective atomic number of the material and define its attenuation of the impinging photons depending on their energy. In a composite material, the effective atomic number is a weighted average of the atomic numbers of all the elements composing it. Most importantly, the attenuation coefficient at single energy is not unique for the material containing different chemical elements and often has very similar values for different structures. Looking at **Fig. 1**, one can see how close together attenuation curves of malignant and fibro-glandular tissues are.
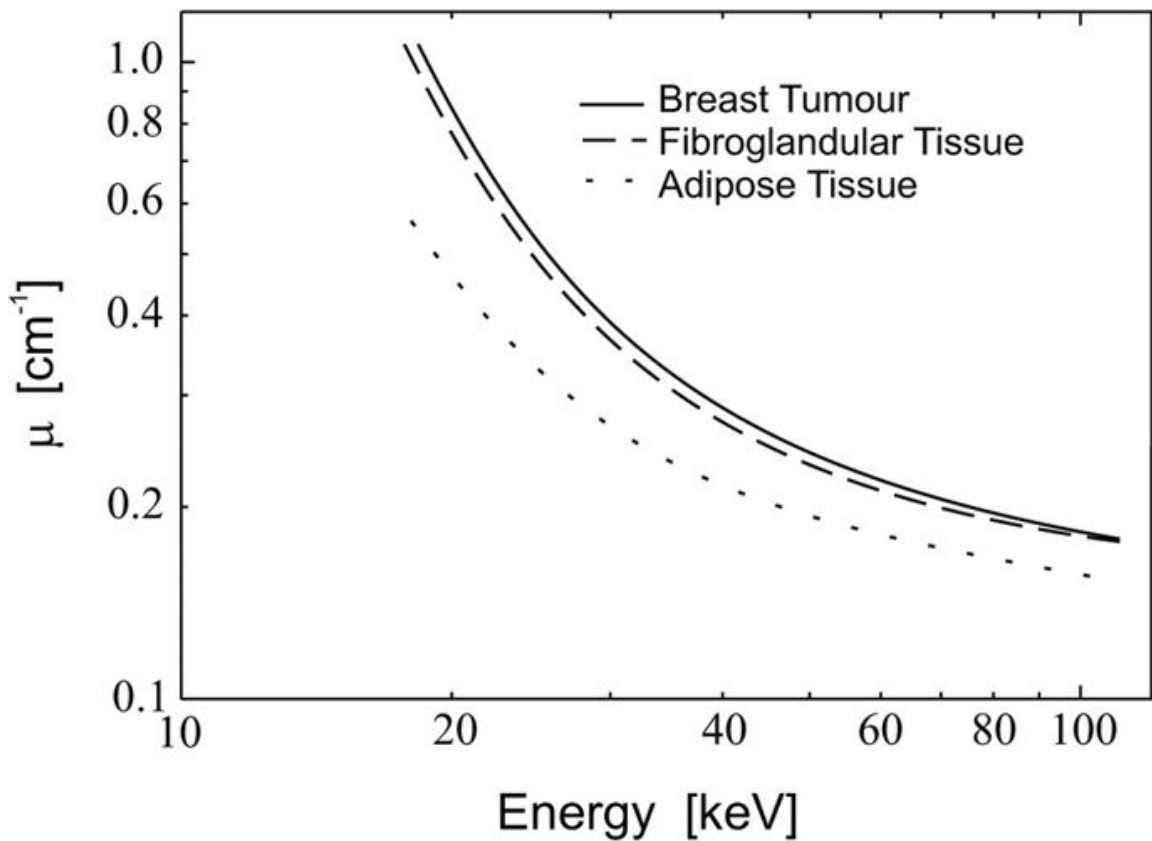
Fig. 1 Attenuation curves for fibro-glandular, adipose and tumorous tissues, Yaffe et al. [4]

Often, based on pure attenuation measurements and in the early stage of tumor development, it is impossible or at least reasonably challenging to distinguish them. Lesions are often present but partially obscured, making it difficult to speculate about their potential malignancy. In contrast to soft tissue, easily visible are calcifications appearing as white specks on the mammogram. Calcifications are small deposits of calcium, and their presence is not necessarily associated with malignancy, although irregular shapes and dense clusters could potentially have further indications.

In the new era of imaging, several modalities have been adopted for breast screening. Each of them has some advantages and disadvantages comparing to each other. The non-ionizing methods make use of ultrasound imaging or magnetic resonance (MR) imaging. Methods relying on ionizing radiation are digital mammography and digital breast tomosynthesis, which completely replaced analog units in recent years. Digital mammography systems are the most comprehensive tool for diagnostic examination and evaluation of breast carcinoma. It represents a golden standard in routine screening.

In most cases, digital mammography is an acceptable 2D imaging method, often accompanied by US examinations and MR imaging on occasion. The main advantages of this technique are low exposure and quick and easy acquisition. The information contained in each pixel is a result of the superimposition of all features of the breast along the path of the x-ray. Digital breast tomosynthesis (DBT) is a step forward to cover this significant drawback and introduce a near 3D acquisition setup. In principle, these machines acquire data positioning the tube and detector at different angles. This data is further processed using tomographic reconstruction methods, which leads to the reconstruction of images in the form of slices. With a set of slices, which could be scrolled through, breast content is disentangled in the vertical direction.

Nowadays, popular accessory to all the mentioned modalities is a computer-aided detection system. At its core, these are machine learning models trained to select suspicious areas on the image to alert radiologists to give them a second look. The sensitivity of algorithms can vary, and it has been shown [5, 6] that architectural distortion in the breast can be detected at a sensitivity level of 49% for one software and 33% for the other. Sensitivity for invasive lobular carcinoma has been estimated in the range from 89% to 100%. Sensitivities for malignances and calcifications are also of a higher level, from 89% to 98% in the first case and close to or even 100% in the second case. At first glance, these systems seem to be an up-and-coming tool for better diagnosis. However, it rarely happens that software does not find any suspicious areas even with healthy breasts. A large study [7] has been conducted examining half a million mammograms failed to find statistically significant improvement in diagnostic outcomes. As for now, available machine learning software is not able to truly improve the diagnostic power.

The ultimate goal of this thesis is to improve tumor delineation at the early stage of its development and therefore improved diagnostic accuracy. Dedicated post-processing methodology was applied to high-quality synchrotron CT images, with the aim of describing image contents in terms of effective number and density. To achieve the goal of the quantitative material description, following tasks had to be assessed:

1. The high-quality images of custom-made, breast tissue-equivalent phantom had to be acquired at various energies
2. The novel theoretical approach had to be derived to decouple the Z_{eff} from a density of each of phantom materials
3. The dedicated software had to be built from scratch, capable of performing the theoretical task on the experimental data
4. The accuracy of the obtained results had to be estimated through the calculation of the corresponding standard error of the values obtained through the applied model

1   Literature review

1.1   Tomography

The development of breast computed tomography (BCT) imaging technique was initiated with the goal of improving sensitivity, especially in dense breasts. Visualization in 3 dimensions, as well as improved, near isotropic resolution, are expected to improve diagnostic outcomes. A few solutions are available and already implemented in clinical practice. Cone beam CT is offered by Koning company and spiral BCT offered by AB-CT companies [8, 9]. The breast in these units is not compressed as opposed to digital mammography but instead maintains its regular shape. Patients who very often see the act of compressing as very painful, benefit from increased comfort. In this setup, they lay in the prone position with the breast centered through the hole in the treatment table. The surrounding unit is very complex, with two crucial parts – x-ray source and a detector, one opposite to the other. During the acquisition in the spiral BCT, the source rotates in a spiral path and emits the x-ray photons of a certain energy range. By adjusting the voltage and current of an x-ray tube, the maximum energy of emitted radiation and the number of x-ray quanta are regulated, respectively. After passing through the object, radiation is collected by the detector. From the information collected, an image is reconstructed as the spatial distribution of linear attenuation coefficients within the breast. The contrast in an image comes from the difference between values of linear attenuation coefficients over various tissues inside the object. Spatial distribution is preserved in the form of voxels, whose size is determined by the slice thickness and number of acquisitions per one full rotation. While the number of projections undoubtedly plays a role, the resolution is the most firmly affected by the pixel size of the detector. Following the convention, attenuation values are transformed into Hounsfield units (HU) and thus put in perspective of water attenuation.

$$CT_{number}(HU) = K\frac{\mu - \mu_w}{\mu_w} \tag{1}$$

An integer constant K is standardized to be 1000. A CT number is seen as a gray level in the image and is equal to zero for water. For materials that attenuate stronger (e.g., calcifications), this number is positive, and they appear brighter than water. And vice versa, for fat tissues or air with lower μ, CT number becomes negative, and they appear darker.

1.1.1   Synchrotron breast CT

In this work, a novel and state-of-the-art breast CT unit developed as an initiative of SYnchrotron Radiation for MAmmography (SYRMA-3D) project was used for data acquisition. The significant difference of this setup compared to the conventional spiral CT unit is in its source of radiation that is coming from a synchrotron. Electrons accelerated to the relativistic energy of 2.4 GeV are forced to move in a circular direction with the help of bending magnets. In the place of such a magnet, electrons are forced to turn and therefore accelerate. They emit electromagnetic (EM) radiation as a result of the rearrangement of the electric field around them. A high flux of photons is further guided to dedicated beamlines. Such a high flux allows for filtration of the photons leaving the monochromatic beam of high spatial coherence and high brilliance defined as

$$brilliance(B) = \frac{photons}{seconds\ mrad^2 * mm^2 * 0.1\%BW} \tag{2}$$

The higher the value of B, the more photons falling within a bandwidth (BW) of 0.1 % are concentrated on the area per unit of time. Filtration of a beam coming from rotation anode in conventional clinical units to achieve the sufficient monochromatic property of the beam simply does not leave it with high enough brilliance to be used for imaging purposes. The system weighting function (SWF) w(E) defined for the polychromatic source as

$$w(E) = \frac{S(E)D(E)}{\int_E S(E')D(E')dE'} \tag{3}$$

is characteristic of every detector D(E) and source S(E). For monoenergetic radiation, the SWF of energy $E=E_0$ becomes the delta function.

$$w(E) = \delta(E - E_0) \tag{4}$$

Measurement of spatial attenuation coefficient $\mu(E,r)$, which stands for ground-truth value, is not possible in general using conventional CT machine. What we obtain is attenuation coefficient $\mu(r)$, where dependence on the energy is inherently coupled to the spatial information. Namely, as already mentioned, the x-ray tube emits photons which do not have all the same energy. Instead, they could have any energy value within the selected range. One of the main advantages of a synchrotron source is the ability to precisely select specific energy with very low dispersion. In this case, integration over energy range is avoided, and attenuation is given by the ratio of intensities I and I_0 as

$$ln(A) = \frac{I}{I_0} = -\int_L \mu(E_0, r)dl \tag{5}$$

where µ depends on both, the energy of the beam and depth of the sample along the path L.

1.1.2 Tomographic reconstruction

When a set of parallel x-rays transverses object of interest, an integral of attenuation coefficients of x-rays in near proximity is assigned to a single pixel in a projection. A single projection of a 2D object is, therefore, one dimensional. A sinogram is a collection of several projections acquired at several angles. Data collected in this way is in a similar form to that described by Radon transform [10]. As in the sinogram created by the CT unit, the Radon transform $R(r,\theta)$ of small objects appears graphically as a number of sine waves of various amplitudes and phases in the vertical direction. In other words, the Radon transform of 2D objects simulates a tomography experiment.

$$R(r, \theta) = \iint f(x, y)\,(x \cos \theta + y \sin \theta - r)\ dx\,dy \tag{6}$$

Here function f(x,y) represents a 2D distribution in the x-y coordinate system, θ is the angle of the projection, and r is the perpendicular offset from the origin. For better understanding, the formula is followed by **Fig. 2**.
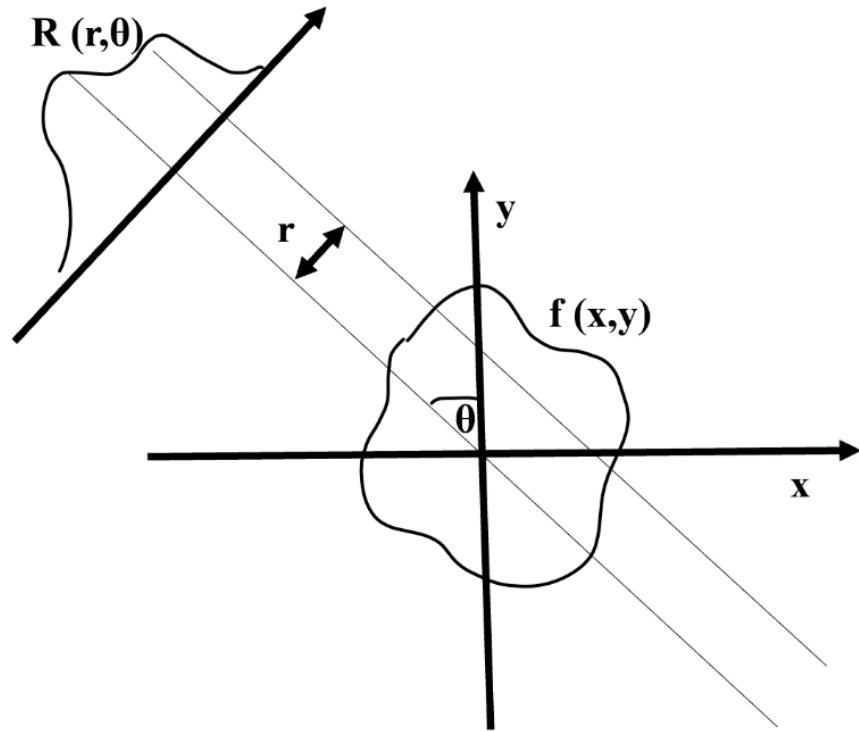
Fig. 2 Visual representation following the equation   (6) for clarification of the Radon transform used for the reconstruction of CT images

Johann Radon also provided the formula for the inverse transform in 1917, which can be used to recover 2D density distribution from multiple projections. Filtered Back Projection (FBP) is the most commonly used method for tomographic image reconstruction and consists of two phases: The inverse of Radon transformation for discrete values and additional filtering. Shepp-Logan and Hann filter are just some of the filters most often used to improve image quality and reduce the artifacts created by the reconstruction process [12]. Required linear physics of equation (6) for transformation and its inverse to recover μ from the sinogram relays on fact that output of synchrotron source is of single energy value, E_0. For conventional machines, an approximation that E_0 is equal to the average energy of the source is used. The price is the formation of artifacts known as the beam hardening effect. When the beam passes through the body, as it penetrates further in the tissue, photons of lower energy are absorbed first. The average energy of the beam moves toward the higher value making the beam "harder." This effect is enhanced in the presence of dense or high atomic number objects (e.g., calcifications). Moreover, beam hardening becomes particularly expressed at the low energies used for breast imaging. Due to the assumption that all the emitted photons have the same energy, attenuation A becomes overestimated and, consequently, effective μ is underestimated in the reconstructed image. Beam hardening corrections are always applied to the reconstructed images and are very successful in modern scanners. They work very well for homogeneous tissues but often fail in the presence of high-density materials. This points out another great advantage of imaging using precisely defined energy values. The beam hardening effects are not of the concern in the synchrotron breast CT.

1.1.3 Detector and pre-processing

Besides beam hardening artifacts, many others occur during the process of image acquisition. These are present even in our experiment and can be corrected with dedicated processing to some extent. Many of them are detector specific, so implementation of pre-processing procedure characteristic for the chosen detector is of high importance. The SYRMA-3D project relays on the Pixirad-8 detector to obtain 'clinical-like' breast images. Pixirad-8 is a novel, large-area CdTe photon-counting detector. The sensitive area with the surface of 246 x 24.8 mm^2 is comprised of 8 modules joint together with an overall matrix dimension of 4096 x 476 pixels. They are arranged in a honeycomb matrix of pixel-to-pixel spacing of 60 μm and 52 μm in the horizontal and vertical direction, respectively. Since each pixel is associated with two independent discriminators, it opens an opportunity to use the detector in dead-time-free mode. While one counter of the pixel is in operational mode, the other is being read, effectively reducing the acquisition time and dose to the patient. Detector yields some common artifacts like the ring or partial ring artifacts and streak artifacts. First are the result of detector inaccuracies such as errors, imbalances, and calibration drifts in an element of the detector relative to its neighbors. Streak artifacts could be caused due to numerous reasons, but most are due to inconsistent or bad detector measurements. All of these and some other artifacts specific for our detector were studied with great care by SYRMA-3D collaboration and assessed in the pre-processing phase before image reconstruction. They are organized in a modular structure comprising of five steps: dynamic flat-fielding, gap seaming, dynamic ring removal, projection despeckling, and around-gap equalization. A detailed description of their cause and technical solutions is beyond the scope of this work, but the interested reader is referred to [12]. Motion artifacts are always present due to normal physiological functions of the patient's body and their intensity differs depending on the part of the body being imaged. In the context of breast imaging, these movements are very intense thanks to their proximity to the heart and lungs. Since breast in BCT hangs with no support, further complications in terms of breast movement are introduced. It is enhanced when the patient support table is rotated instead of the x-ray source to acquire images at various angles. This setup is convenient for synchrotron radiation breast CT. However, in this case, the inertial movements occurring when table changes direction could be a possible source of artifacts. These movements are predictable and could be eliminated with image processing tools.

1.2 Phase-contrast imaging

The linear attenuation coefficient is just one piece of information carried by the content of the beam. It is a quantity describing how much some material attenuates the x-ray beam impinged upon it. Besides, in the process of interaction, the electromagnetic wave changes its phase. The wavefront of the same beam is phase shifted from the initial phase. This phenomenon is used in many applications such as light microscopy and transmission electron microscopy. In the x-ray tomography, it is used to increase image contrast by highlighting the regions of differing refractive index within the structures. For a breast, which consists of low atomic number tissues, phase contrast imaging is more sensitive to density variations than transmission-based X-ray imaging. Since refractive index difference is the largest at the edge of two different tissues, phase contrast imaging leads to consequentially edge enhanced images.
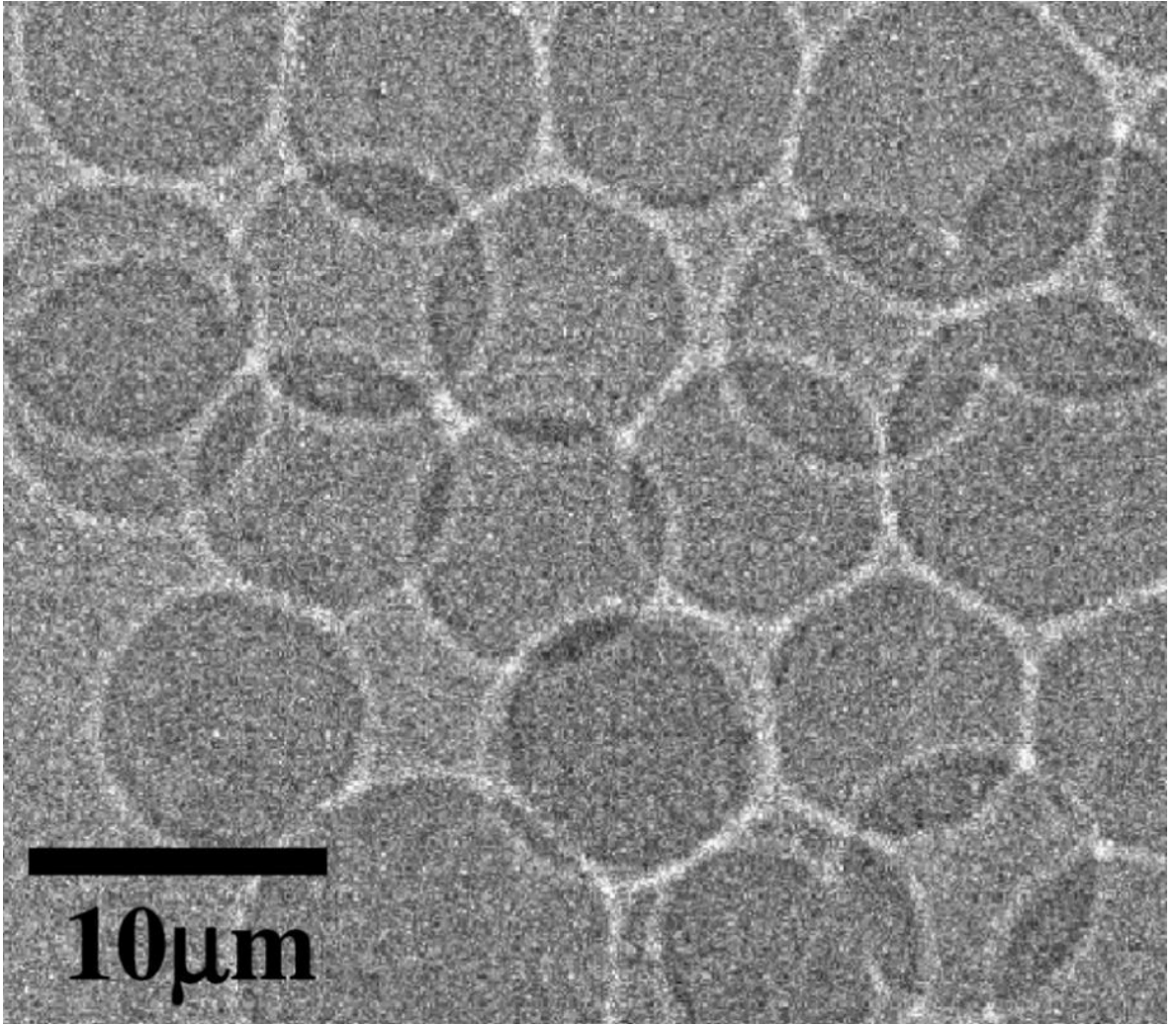
Fig. 3 Phase-contrast x-ray images of latex spheres, Paganin et al. 2002 [13]

The full potential of CT imaging (and other radiation methods as well) lies in exploiting all the information contained inside the beam. Beam's behavior when passing through the object is entirely described by the refractive index n of that object. It is a complex quantity defined as

$$n = 1 - (\delta - i\beta). \tag{7}$$

The information used by most of CT scanners, μ, is hidden in the imaginary part of this equation and β is in simple relation to μ as

$$\mu = \frac{4\pi\beta}{\lambda} \tag{8}$$

where λ is the wavelength of source output. The real part of the equation (7) is related to the electron density ρ_e and dependents on the energy E as

$$\delta = \frac{\rho_e r_0 \hbar^2 c^2}{2\pi E^2} \tag{9}$$

where r_0 is the classical radius of the electron, and ℏ and c are reduced Plank constant and speed of light, respectively. The value of the real part δ is related to the phase shift effect and can be determined only thanks to a specific acquisition setup [13, 14, 15]. Once measured, it can be used to calculate

the electron density of each voxel. Extensive research has been conducted in recent years to extract the effective atomic number Z_{eff} from μ using this information [16, 17]. Effects causing phase shifting are entirely independent of the effects causing beam attenuation. This independence of two different channels of image formation opens up a possibility of further manipulation with the ultimate goal of separating materials that would produce the same gray level in pure attenuation imaging. Otherwise indistinguishable, materials can be seen as different based on other criteria (e.g., effective atomic number or density). Although this work shares the same effort, the proposed method seeks the independence of information from image acquisition at various beam energy values. Quantitative evaluation and decoupling of the effective atomic number and density assessed in this work will be described in the next section. Nonetheless, phase shifting phenomena is beneficial and well exploited in SYRMEP-3D beamline to drastically increase the image quality. Placing the detector very close to the object would result in contrast coming from attenuation differences. On the other hand, moving the detector further away will allow for additional contrast enhancement coming from the difference in the phase of incoming waves. This leads to a substantial improvement of small and low contrast details visibility.

1.2.1 Phase retrieval

High brilliance of synchrotron source allows the distancing of detector significantly further away (a few meters) from the source of radiation and letting the beam propagate in free space. The real part of the refractive index of visible light can be very variable (e.g., n for glass materials is in the range from 1.5 to 1.8), but for x-rays, these variations for different mediums are of the order 10^{-5}. Consequently, the refraction angles caused at the boundaries of the two regions are minimal as well. A large object to detector distance allows for the creation of interference patterns of refracted waves. The free-space propagation is essentially an optical convolution in a forward direction. It can be mathematically formulated as

$$1 - \sigma^2 \nabla^2 = 1 - \frac{\lambda R_2 \delta}{4\pi\beta} \nabla^2 \tag{10}$$

using the 'Transfer of Intensity Equation.' The transverse spread of phase contrast is σ, λ is a wavelength, R_2 is an object to image distance, and ∇^2 Laplacian over the transverse dimensions. Retrieved image is obtained by applying precisely the opposite kernel from the one in equation (10). In this two-step procedure described by Paganin et al. [13], physical forward propagation is followed by backward numerical deconvolution, referred to as the phase retrieval kernel. A great visual representation of this idea was given by Piai et al. [18].
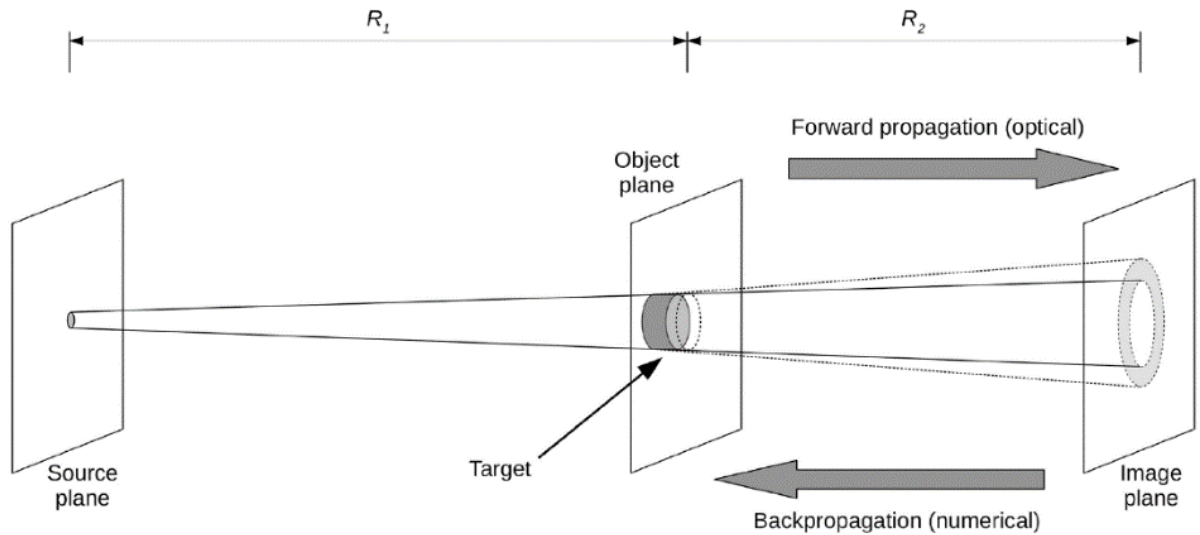
Fig. 4 Schematic representation of experimental setup: an edge enhancement of an object is visible in the imaging plane. The beam propagates in the free space before reaching the detector. The numerical deconvolution is used to retrieve resulting gray levels in the image [18]

Here, R_1 stands for the source-to-object distance, which determines the spatial coherence of the beam. Since phase contrast was gained and subsequently subtracted, the outcome is formally a pure attenuation image. The described method significantly increases the signal-to-noise ratio (SNR) while preserving spatial resolution. At first glance, this seems to violate the fundamental nature of the trade-off between the SNR and spatial resolution. Improved spatial resolution, in other words, means fewer photons scattered by the smaller volume which lowers the intensity of the collected signal and therefore lowers signal to noise ratio as well. The extensive theoretical clarification of seemingly "unreasonable" significant improvement of image quality is given by Gureyev et al. [19]. The noise content of an image remains unchanged during the free-space propagation. This is true because noise is generated at the moment of image detection and is not propagated by the optical convolution. At the same time, applying a mathematical deconvolution leads to a significant reduction in noise variance and SNR increase, as it is expected from any numerical convolution. Leaving the dose to the breast and the time of acquisition unchanged, signal to noise ratio is improved proportionally to the increment of the object-to-detector distance. Further, doubling the dose at constant distance R_2 would increase SNR four times, leading to a significant improvement in image quality. The price is not paid in loss of spatial resolution since two steps of a forward and backward convolution are inverse to each other. Spatial resolution is improved during optical propagation and is consequently returned to the original level during numerical backpropagation. High-quality images produced by synchrotron CT are suitable for a dedicated post-processing method developed in this work.

1.3 Radiation interaction with matter

When x- or γ-ray encounters an object, three possible outcomes are going to occur. The radiation will be either transmitted, without any interaction, or it will interact with atoms or molecules of media that it is traveling through. In the case of interaction, photons can be scattered in one or two interactions or absorbed (i.e., energy is transferred to the atoms of media). For a later description of material decomposition algorithms used as a tool of tissue discrimination, it is necessary to take a closer look at mechanisms of radiation interaction. For the narrow monoenergetic beam containing no scattered photons, equation (5) can be rewritten in more familiar form as

$$I = I_0 e^{-\mu\, l} \tag{11}$$

with all the symbols having the same meaning as stated before. The $e^{-\mu l}$ term describes the probability that the photon transverses the material of thickness l without any interaction. It is equal to the probability that the photon does not interact with the material through any of the four known physical processes occurring in diagnostic imaging. Therefore, this probability is equal to

$$e^{-\mu\, l} = (e^{-\omega\, l})\,(e^{-\tau\, l})\,(e^{-\sigma\, l})\,(e^{-\kappa\, l}) = e^{-(\omega+\tau+\sigma+\kappa)\, l} \tag{12}$$

where ω, τ, σ, and κ represent the attenuation coefficients associated with coherent scattering, photoelectric absorption, Compton scattering, and pair production. In some cases, it is of interest to exclude scattered energy and determine only the amount of absorbed energy. The absorption coefficient is given as

$$\mu_{en} = \mu\frac{E_a}{h\,v} \tag{13}$$

where E_a is an average energy per photon interaction and hv is the photon energy. Dividing the absorption coefficient with the density of medium leads to the mass-energy absorption coefficients denoted as μ_{en}/ρ. These definitions are useful for the understanding of **Fig. 5** with energy attenuation and absorption coefficients for air, as a function of photon energy.
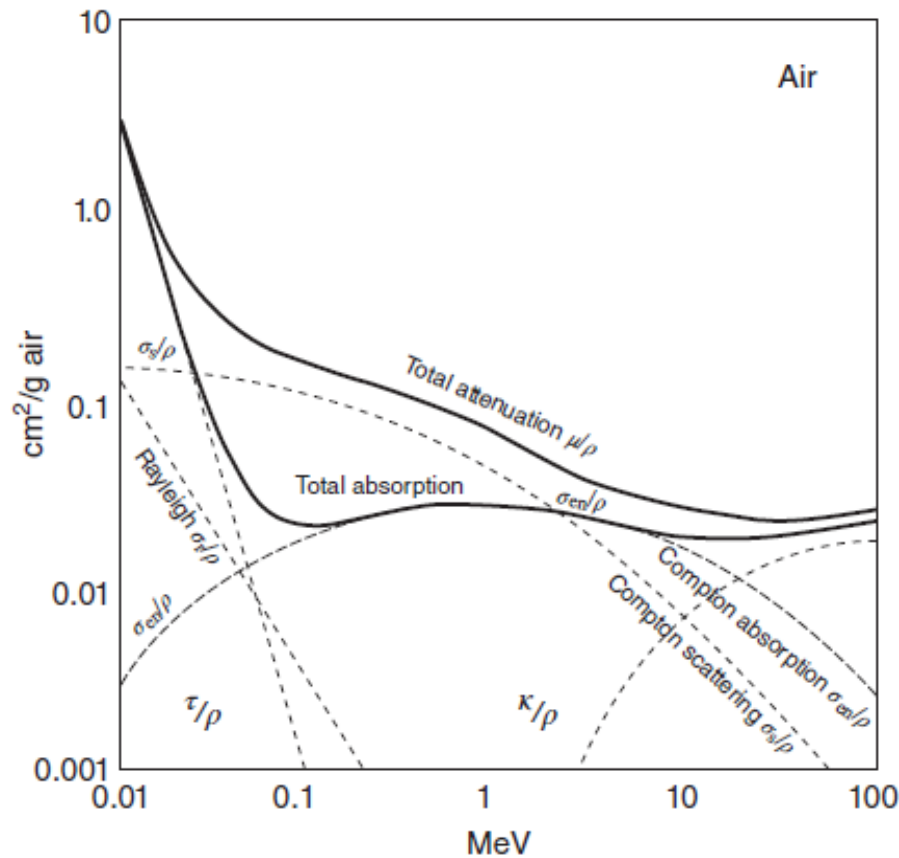

Fig. 5 Mass attenuation coefficients for the photons in the air resulting from underlaying physical processes during photon-air interaction [12]

The total absorption is always lower than total attenuation since every material produces some number of photons scattered from the beam. In **Fig. 5**, all the contributions to the attenuation are seen,

but the curve for total absorption is a product of only three absorption effects: photoelectric, Compton and pair production.

1.3.1 Rayleigh scattering

Rayleigh or coherent scattering is a scattering process of negligible loss of energy. It is an interaction of a photon with electrons of an atom as a group rather than individual electrons. It can be described by classical physics, so it is often referred to as classical scattering as well. Since the photon in the case of classical scattering "sees" an atom as a whole, it is more of molecular scattering. Photons interacting with molecules are preferably scattered in the forward direction and are mostly used for studying of the crystalline structure of the material. Their contribution to the image formation in medical imaging is subdominant to all the other effects and encounters for less than 10 %.

1.3.2 Compton scattering

Compton effect is a predominant physical interaction mechanism for a wide range of energies, starting from around 30 keV for the low Z materials composing soft tissue. In the conventional imaging systems, which often operate in ranges a bit higher than this value, contrast, therefore, is mostly created due to the Compton attenuation. In SYRMEP breast CT, some images were acquired at energies lower than 30 keV, leading to contrast coming from photoelectric attenuation. The predominance of the two effects at certain energy depends very much on the effective atomic number of the material photons are interacting with. During a Compton interaction, energy is transferred to a loosely bound (or free) electron within the attenuator. Since binding energy (i.e., the minimum required energy to be transferred to an electron to set it free) is negligible, the kinetic energy of the recoil electron is equivalent to the energy lost by the photon. Compton (recoiled) electron is scattered at any angle θ between 0 and 90 degrees with respect to the direction of the incident photon. On the other hand, the photon can be scattered at any angle α.

$$\Delta\lambda = 0.00243\,(1 - \cos\alpha) \tag{14}$$

The change in photon wavelength $\Delta\lambda$ in nm is the largest when α = 90 degrees – the greater the energy transfer is, the more recoiled electron will be scattered away from the photon's initial direction. Because photons preferably interact with loosely bound electrons, Compton attenuation leaves us with the map of electron density of the material. Opposing to photoelectric attenuation, Compton scattering is nearly independent of the effective atomic number. Because of this contrast coming from high energy x-rays is very poor. The image reflects differences in physical density between different regions.

1.3.3 Photoelectric effect

The photoelectric effect was mathematically described by Albert Einstein in 1905. The total energy of the photon is transferred to the inner electron of an atom. The highest probability for the photon is to interact with an electron on the path closest to the nucleus – the electrons on the innermost shell. These electrons have the highest binding energy E_b which decreases in value for electrons on the upper shells. When a photon of energy hν interacts with one of the electrons, it sets it free from the influence of the nucleus giving it kinetic energy of

$$E_k = h\nu - E_b \qquad (15)$$

The average binding energy for the innermost shell (the K shell) electron in soft tissue is approximately 0.5 keV [12]. For the breast images acquired at the energy of 28 keV, the ejected photoelectrons will be of the energy 0.5 keV less than this value. Also, at these energies, the preferable emission of electrons will be at the right angles (90 degrees) concerning the initial beam orientation. At the moment of emission, the atom becomes unstable, and immediately, the hole is filled with the electrons from the upper shells. It most often happens in forms of cascades, where electron from the next shell fills the hole in the last one. The excess of energy is released in the form of characteristic photons and Auger electrons possessing energy less than 0.5 keV in soft tissue. Consequently, these low energy photons and electrons are absorbed rapidly by the surrounding tissue. Since photon energies are very low and hence quickly absorbed, the beam must be of a high fluence so that enough photons are collected on the detector distinguishing the source of interaction from the stochastic noise. Imaging at low energies to target the photoelectric effect produces high-quality images with good contrast. The photoelectric mass attenuation coefficient depends on the effective atomic number as $Z_{eff}{}^3$ for elements composing organic tissues. This value for adipose tissue is Z (adipose) = 6.47 and for compact bone is Z (bone) =12.31 [20]. The number of photons absorbed by the photoelectric effect in the bone is $(12.31/6.47)^3$= 6.88 times greater than the number of photons absorbed in the equal mass of the adipose tissue. This is a principal reason for the usefulness of low-energy x-rays in an imaging application. In mammography, very often are used contrast agents of high atomic number. These are injected for better visualization of tissues producing the same attenuation. One of most often used are iodine and barium with K-edges at energies of 33 and 37 keV. Edges are discontinuities in the attenuation curve at the photon energy equal to the binding energies of the electrons in inner electron shells. For photon energies higher or the same to the binding energy of K electron, the probability of photoelectric interaction with this electron is high. When energy drops below this value, photons interact predominantly with electrons in the next shell. If energy decreases further, the only possible interaction is with electrons in the next shell further away from the nucleus, and so on.

1.3.4   Pair production

Pair production describes the process of electron-positron pair creation in the near proximity of the nucleus. Because the resting energy of electron and positron is 511 keV, the minimum photon energy required to create such a pair of particles is 1.02 MeV. Such energies are not used in conventional radiographic imaging and are far above energy values used in for image acquisition described in this thesis. Under the assumption that Rayleigh scattering has very little influence that can be neglected and that photodisintegration requires energy higher than that for pair production, the rest of the three effects are shown in **Fig. 6**.
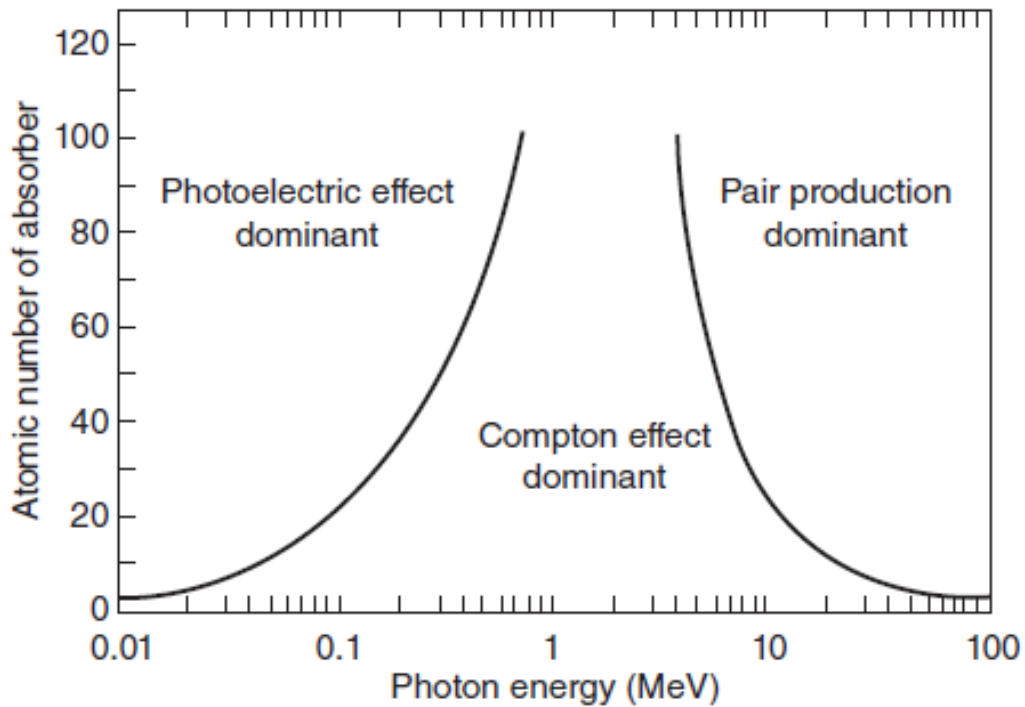
Fig. 6 Predominance of the photoelectric effect, Compton scattering and pair production depending on the photon energy and effective atomic number of absorbing medium

For low energy values (below 30 keV) and high Z materials, the x-rays are predominantly attenuated through photoelectric attenuation. As energy increases, the attenuation dominance is established by the Compton (incoherent) scattering effects. Energies at the MeV level are irrelevant for imaging purposes.

1.4 Spectral CT

1.4.1 Technical approaches

In the same way, phase-contrast image and attenuation contrast form two independent channels of image formation; this independence could be achieved by image acquisition at different energy values. The phase-attenuation combination came many years after the first ideas for the construction of dual-energy CT. In this work, the theoretical derivation and following experimental work lay its roots on the ideas proposed in the late seventies of the last century [21, 22]. As it often happens in the field, theoretical ideas were developed early but had to wait some time to be applied. Nowadays, dual-energy CT solutions are quite common in clinics with many practical applications. Standard techniques are rapid keV switching using one source or availability of dual x-ray source geometry, where tubes are offset for 90 degrees with corresponding independent detectors. Independent data can also be acquired from the perspective of detector advances. In pair with a single high tube potential beam, layered scintillation detectors are used. The first layer on the surface of the detector is reserved for low-energy data, while x-rays of higher energy with more penetration power are collected in the second layer behind the first one. The simultaneous data acquisition removed the co-registration errors between high and low- energy images that often occurred due to the patient's movement. The last of technical solutions, the dual-x-ray source CT was initially introduced in 2006. Images acquired this way are used to perform material decomposition analysis in the image domain [23]. Material decomposition is a technique where each image is represented based on usually two

materials. Since the main goal of this thesis is exactly the development of such a technique, the whole another paragraph will be dedicated to its discussion. The most robust solution is a photon-counting detector capable of counting discrete photon interactions. Their implementation in the clinical environment is at the stage of research, although they are used in nuclear medicine and spectral mammography. Photon counting detectors are often adopted for a certain application. One approach is to use a detector with two or more channels, where the upper boundary of one channel is set to lower energy value than others. This method is popular for spectral imaging with a polychromatic source. The other approach is to use the full potential of the detector but acquire two separate images at different beam energy values. During acquisition, data is collected without any losses since there is no detector "dead" time. While one channel is being discharged and insensitive, the other channel is active and collects the incoming radiation. Such detector mode is used in the SYRMA-3D collaboration since the source of radiation is monochromatic. In case splitting the detector in multiple channels, photon fluence per channel is reduced, leading to increased noise, but in case separate image acquisition difficulties may arise in the co-registration of two images. So far, the research is focused on the phantom study with a transition to the breast mastectomies. With no concerns regarding motion artifacts, the attention is only paid toward the positionally correct start of the acquisition. Namely, each acquisition must be initiated in the same position as the previous one. This leads to perfectly aligned pixel positions for each stack of images. Synchrotron radiation breast CT is capable of the acquisition of multiple images of the same sample slice but at different energies. Four separate image acquisitions were performed with energy values of 25,28, 32, and 35 keV for the needs of this work. Since noise contribution in an image is randomly distributed, the overlapping of four images further reduces the noise content of an image. Collected multi-energy, high-quality images with excellent contrast and high SNR are of great importance for the understanding of proposed theory and initial testing.

1.4.2 Physical approach

Every individual pixel of an image is assigned with a linear attenuation coefficient $\mu(E)$, which is not unique for any given material but is a function of the photon energy interacting with the material and its material density and composition. Therefore, it is useful to factor spectral attenuation coefficient into density ρ and mass attenuation coefficient $\mu_m(E)$. Mass attenuation coefficients are obtained by dividing the linear attenuation coefficient by the density ρ of the absorber. It is a characteristic function for each chemical element with an atomic number Z.

$$\mu_m(E) = \left(\frac{\mu(E)}{\rho}\right)$$

(16)

The fact is that μ_m cannot be measured but only calculated. Even for the case of a single element material, density and atomic number information are heavily coupled and cannot be determined with a simple measurement. But attenuation curves for elements in the periodic system are well known and produce distinguishable gray levels. However, organic tissues are mixtures of elements, and their attenuation is given as

$$\mu(E) = \rho\,\mu_m(E) = \sum_{i=1}^{m} \rho_i\,\mu_{m,i}(E)$$

(17)

Spectral attenuation for a mixture of m materials can be computed as the sum of all contributions weighted by the partial densities ρ_i (in g/cm^{-3}) of each material inside the mixture. Very often, one material with ρ_1 and $(\mu/\rho)_1$ and other material with ρ_2 and $(\mu/\rho)_2$ could produce nearly the same linear attenuation coefficient at the diagnostic energy range. The typical example is difficulty in differentiating calcified plaques and iodine-containing blood. Note that iodine has Z of 53 and calcium Z of 20. Besides, glandular tissue and developing breast carcinoma are also prone to causing such indistinguishable attenuations.

The full potential of spectral CT imaging is exploited with the development of dedicated algorithms. They intend to distinguish materials that yield the same values of CT numbers. Sometimes it is enough to acquire two independent images, one at low energy and one at high energy. This approach relays on the energy dependence of the underlying physical attenuation phenomenon. At the lower energies, the contrast resulting predominantly from photoelectric attenuation will be profoundly affected by the effective atomic number of the tissue. In the case of two tissues, these values are different, and it will lead to discrepancies between their attenuation curves in the lower energy range (typically in range less than 30 keV). On the other hand, if there exists a difference in electron density of the two regions, it will be better seen in the high energy image where Compton scattering dominates. So, we are given an opportunity to look at the photoelectric attenuation weighted image and Compton attenuation weighted image. The contrast between previously indistinguishable regions in some energy range becomes visible. Of course, these images are further processed with computational segmentation algorithms. They are often enough for the task of separating materials which do not have a very similar effective atomic number. An example is the separation of bone and blood mixed with iodine contrast, which produces almost the same linear attenuation coefficient at the energy of 100 keV, but not at other energy values.
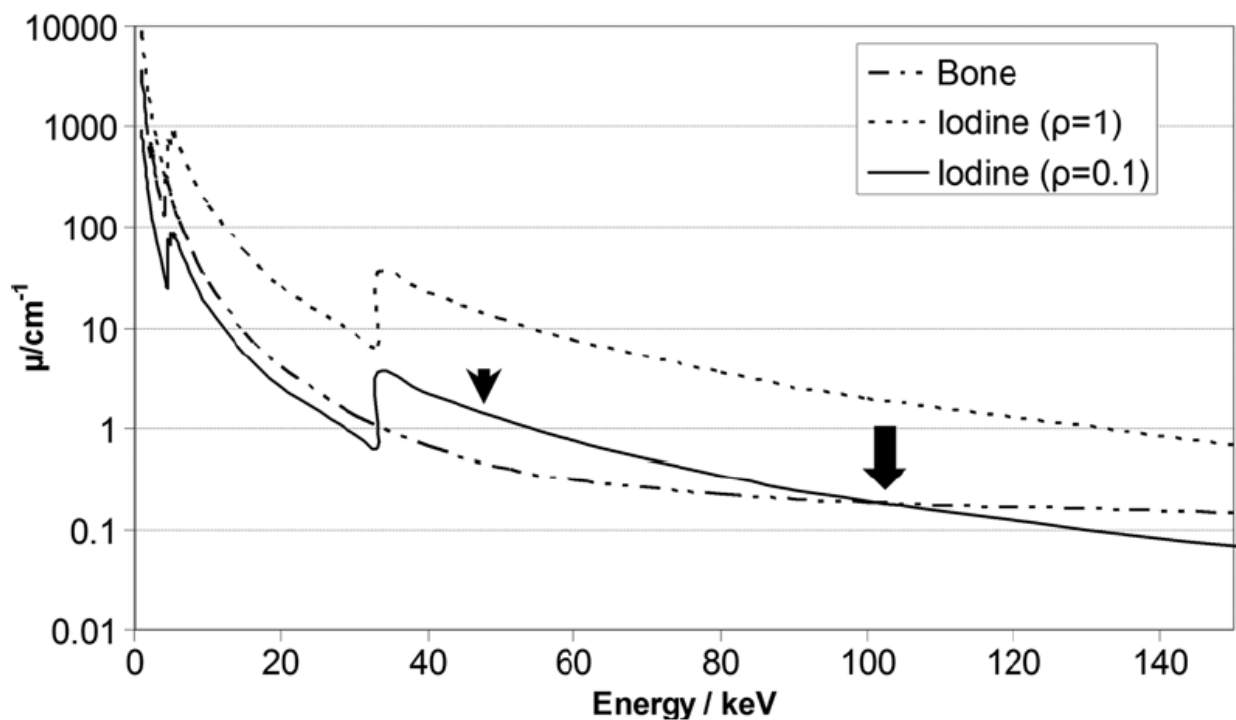

Fig. 7 Linear attenuation coefficients for bone, iodine, and iodine with a lower density over the diagnostic energy range [23]

Dual-energy CT is often used for K-edge imaging to detect specific or even multiple contrast agents. It involves two energy bins on both sides of the K-edge. The wider the energy bins are, the less noise contribution will be present. However, wide energy bins degrade the contrast on the reconstructed images. Spectral CT has many useful applications such as automated bone removal in CT angiography, blood perfusion CT, virtual non-contrast enhanced imaging, urinary stone characterization where discrimination is based on the detection of uric acid or non-uric acid stones.

Synchrotron radiation (SR) CTs are very rare, but they can have a very sophisticated application. For instance, they are used for obtaining quantitative information about electron density with application to treatment planning for image-guided proton radiotherapy [24]. In this work, an effort has been made toward characterizing all the breast tissue-like materials by its density and effective atomic number.

1.5   Material decomposition algorithms

When both the composition and density are very similar, more advanced algorithms are needed. For separation of glandular and malignant tissue algorithms yielding quantitative information gives much better results. Precisely, quantitative description means decoupling concentrations, atomic numbers, or densities and interpreting them as independent values. The first such algorithm was proposed in 1976 by Alvarez and Macovski [21]. Their work set foundations for the development of basis material decomposition algorithms. They rely on the well-known physical effects occurring during the interaction of radiation and matter. The attenuation coefficient of a generic material can be expressed as the superposition of different effects contributing to the attenuation as:

$$\mu(E, r) = a_1(r)f_1(E) + a_2(r)f_2(E) + a_3(r)f_3(E) + a_4(r)f_4(E) \tag{18}$$

The idea is to decompose an image in two or more images relative to the photoelectric, Compton, or other contributions. Therefore, { $f_1, f_2 \ldots f_4$ } represents exactly these elementary attenuation functions described previously. Coefficients { $a_1, a_2 \ldots a_4$ } are weights of a linear combination of these functions and represent the partial density of each contributing element. For the reasons already mentioned, at the diagnostic energy range, attenuation can be almost wholly described considering the photoelectric (PE) effect and Compton scattering (CE). The mass attenuation coefficient of the two principal means for the x-ray attenuation can be expressed as

$$\frac{\mu(E)}{\rho} \sim a_{PE}f_{PE} + a_{CE}f_{CE} \tag{19}$$

where coefficients a_{PE} and a_{CE} are weights of the mathematical functions f_{PE} and f_{CE} representing the photoelectric effect and Compton scattering, respectively. The linear combination of these two contributions is used to represent each pixel in the original image. Coefficients a_{PE} and a_{CE} are characteristic for the generic material, and a_{CE} is the electron mass density [22].

$$a_{CE} = \frac{Z}{A}N_A \tag{20}$$

Here N_A stands for Avogadro's number, and Z and A are the atomic number and mass, respectively. Function f_{CE} is the Klein-Nishina function

$$f_{CE}(k) = C_0 \left\{ \frac{1+k}{k^2} \left[\frac{2(1+k)}{1+2k} - \frac{1}{k} \ln(1+2k) \right] + \frac{1}{2k} \ln(1+2k) \right.$$
$$\left. - \frac{1+3k}{(1+2k)^2} \right\} \tag{21}$$

where $k = E \big/ 510.957 \, keV$ and $C_0 = 2 \pi \left[\frac{\mu_0 \, e^2}{4 \pi \, m} \right]^2 = 2 \pi \, r_0^2$.

The exact mathematical description of the photoelectric effect does not exist, but it is rather empirically described. R.E. Alvarez [21] with his colleagues proposed the definition of the PE as

$$a_{PE} f_{PE} \sim K_1 \frac{\rho}{A} \frac{Z^n}{E^3} \tag{22}$$

where K_1 is a constant, and n $\sim$ 4. This formulation will later be used as a starting point in our theoretical derivation. A similar definition of the photoelectric effect was published in [22].

$$a_{PE} f_{PE} \sim a_c \, C_p \frac{Z^{3.8}}{E^{3.2}} \tag{23}$$

Here Cp = 0.8 x 10^{-24} and E is in keV. Contrary to the linear attenuation, every material is uniquely characterized by its values a_{PE} and a_{CE}.

1.5.1 Two-dimensional approach

The material decomposition approach could be applied to plain, two-dimensional x-ray images. When attenuation is measured at two energies (E_i and E_j), then for object thickness L it is described as

$$\ln(\mu(E_i)) = (a_{PE} \, f_{PE}(E_i) + a_{CE} \, f_{CE}(E_i)) \, L \tag{24}$$

$$\ln(\mu(E_j)) = (a_{PE} \, f_{PE}(E_j) + a_{CE} \, f_{CE}(E_j)) \, L. \tag{25}$$

Here, the two independent energy information allows for the calculation of two unknowns a_{PE} and a_{CE}. In other words, solving the two equations identifies the unknown material. The result of such calculation for each pixel separately leaves us with two completely new images in terms of a_{PE} and a_{CE}. Image "a_{PE}" is an image of the PE, and image "a_{CE}" is an image of the CE contribution. Measurements at more than two energies add no new information since resulting equations would be linearly dependent. Also, functions f_{PE} and f_{CE} do not need to be a mathematical construct. Instead, they can be linear attenuation coefficients of natural material. These materials are called basis materials because they can be used to describe all the other materials. The analog to equation (19) for the case of attenuation curves of physical material is

$$\frac{\mu_u(E)}{\rho_u} = x_1 \frac{\mu_1(E)}{\rho_1} + x_2 \frac{\mu_2(E)}{\rho_2} \tag{26}$$

where 'u' is denoted unknown or generic material and with '1' and '2' two chosen basis materials. Very conveniently, when the 2D imaging approach is considered, the attenuation of unknown material can be described as the ratio of relative thicknesses of two known materials. Replacing the equation

(26) for the real physical attenuators into (24) and (25) leads to the

$$\ln\left(\frac{\mu_u(E_i)}{\rho_u}\right) = x_1 \frac{\mu_1(E_i)}{\rho_1} L_1 + x_2 \frac{\mu_2(E_i)}{\rho_2} L_2 \tag{27}$$

$$\ln\left(\frac{\mu_u(E_j)}{\rho_u}\right) = x_1 \frac{\mu_1(E_j)}{\rho_1} L_1 + x_2 \frac{\mu_2(E_j)}{\rho_2} L_2 \tag{28}$$

The equations (27) and (28) state that generic material of thickness L can be described as a sum of one basis material of thickness L_1 and another basis material of thickness L_2, so that $L=L_1+L_2$. The detected signal in the detector would be the same for generic material and the equivalent combination of basis materials of the same total thickness. It holds regardless of incident photon energy (or spectrum) and detector response [22]. In many studies [22, 25, 26] assessing this thematic, it is common to express the thicknesses and composition of generic material in terms of the vector with magnitude r and angle θ in the basis plane.

$$r = \sqrt{A_1^2 + A_2^2} \tag{29}$$

$$\theta = tan^{-1}\left(\frac{A_1}{A_2}\right) \tag{30}$$

Here vectors A_1 and A_2 are defined as

$$A_1 = x_1 L \frac{\rho_u}{\rho_1} \tag{31}$$

$$A_2 = x_2 L \frac{\rho_u}{\rho_2} \tag{32}$$

Magnitude r is proportional to the thickness of sample L and density of the sample, while angle θ is independent of sample thickness and is related to the effective atomic number of the material. Several studies [25, 26, 27] were published utilizing this technique for the characterization of glandular, adipose and malignant breast tissues. Much of cancer screening relays on mammograms of high resolution for the detection of small calcifications in many of the malignant lesions [21]. Still, applying the spectral technique described above for the application of the clinical breast screening is inexistent. This is mostly due to the fact that thickness L of the breast that beam transverses has to be a priori known or measured during the treatment.

1.5.2   Material decomposition algorithms in tomography

Computed tomography resolution is by far inferior to the conventional or digital mammography, but the necessity of thickness measurements is safely removed by scanning the sample at various angles and use of an appropriate reconstruction procedure. As previously addressed, CT units measure line integrals of the linear attenuation coefficients

$$\ln(A) = \int_L \mu dl = f_1 \int_L x_1 dl + f_2 \int_L x_2 dl \tag{33}$$

where f_1 and f_2 again represent linear attenuation behavior of the two basis materials. The reconstruction of two unknowns, x_1 and x_2, requires two independent pieces of information at every

point along the line of integration. These can be two distinct energies provided by spectral CT unit or independent acquisition of attenuation and phase-contrast information. In this case, x_1 and x_2 are quantities of two materials present in each voxel so that outcome is the same attenuation power as in original (generic) material. These quantities are amounts of materials "squeezed" inside the voxel, and they do not necessarily add up to 1. The choice of a basis materials is empirical, and various possible combinations were tried so far, among them water and bone (WB), water and iodine (WI), water and adipose tissue (WA), and others. One of the choices for a pair of a basis materials is also aluminum (Al) and polymethyl methacrylate (PMMA). The linear attenuation curves of these materials are shown with respect to the other biological tissues.
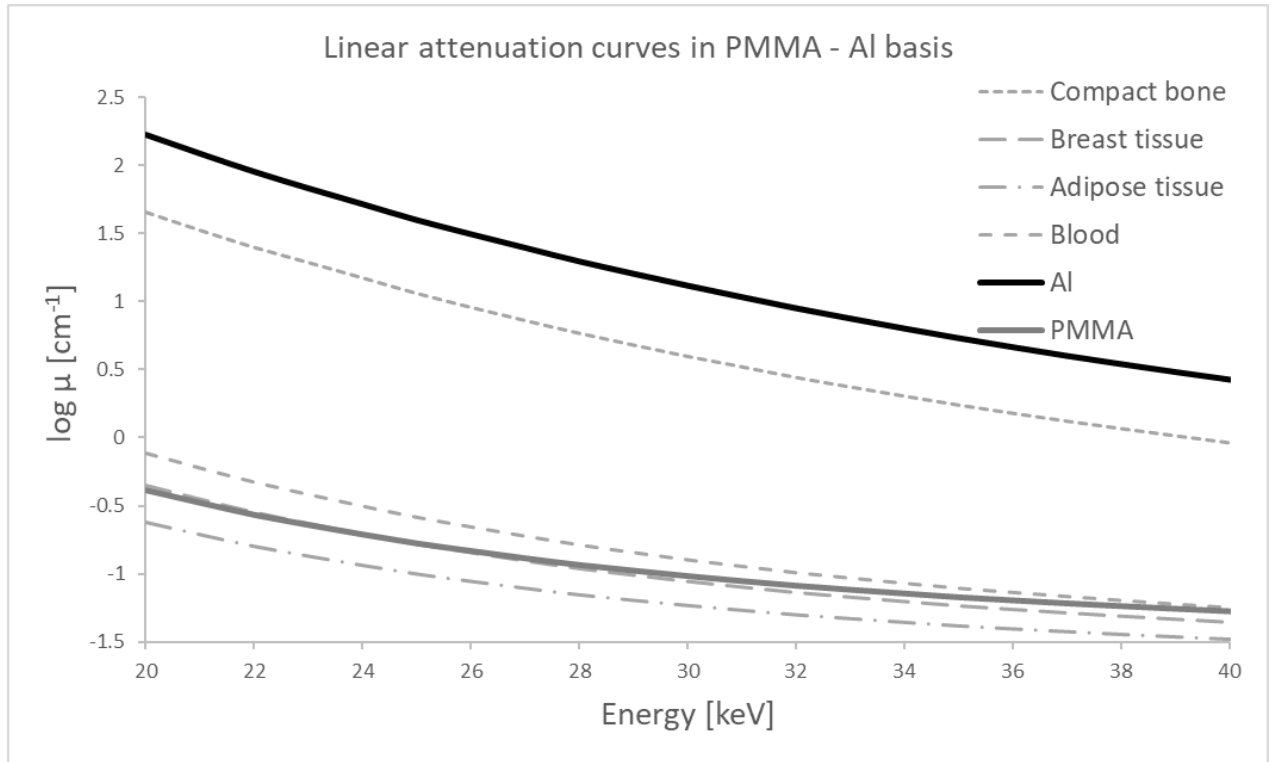
Fig. 8 Logarithmic values of linear attenuation coefficients for various tissue types in relation to the basis materials PMMA and Al, versus energy range of the interest (database [20])

Using the method of least square fit, the attenuation curves of breast tissue, blood, adipose tissue, and compact bone are decomposed in the PMMA – Al basis (PA). Fitting routine is used to find the best linear combination of the two attenuation curves at each available discrete energy value, which will most accurately match the generic tissue's original attenuation at those (and hopefully all other) energy values.

$$y = min \sum_{i=1}^{m} \left(f_{tissue} - \left(x_i \mu_{i,PMMA} + x_i \mu_{i,Al} \right) \right)^2 \qquad (34)$$

In this example, m=2 represents the two basis materials PMMA and aluminum. For the successful fitting, the number of energies must correspond to at least the number of basis materials used to describe the attenuation coefficient of generic material. However, the acquisition of a higher number of images at different energies and using only two basis materials contributes to the accuracy of the fitting method.

Therefore, the objective of this thesis is the implementation of a material decomposition technique for the quantitative examination of breast phantom content. Firstly, the optimal pair of basis materials giving the best result had to be selected. Then, a novel set of transformations was applied on basis materials to decouple density and an effective atomic number of materials composing a breast-equivalent phantom. These are theoretically derived non-linear transformations that are based on certain assumptions applicable to diagnostic imaging energy level and low-Z breast tissues. In parallel, dedicated software was created capable of performing a proposed transformation on breast phantom CT images. The significant contribution to the success of this method was the development of the phantom and the availability of high-quality images of the same phantom. These are the curiosity of the SYRMEP research team at the Italian synchrotron facility, Elettra-Sincrotrone Trieste.

2 Materials and Research methods

2.1 Theoretical derivation of the decomposition algorithm

The first function describing the linear attenuation coefficient proposed by [21] was the sum of empirical relation for the photo effect and Klein-Nishina formula describing Compton scattering.

$$\mu(E) = a_{PE}\frac{1}{E^3} + a_{CE}f_{CE}(E) \tag{35}$$

Therefore, an idea of the basis material decomposition started with virtual, purely mathematical 'materials' which simply describe two different contributions to the attenuation process. In the above formula, only energy dependencies of the mentioned contributions are given. Coefficients a_{PE} and a_{CE} depend on physical parameters as:

$$a_{PE} \sim K_1 \frac{\rho}{A}Z^n; \; a_{CE} \sim K_2 \frac{\rho}{A}Z \tag{36}$$

Here Z is the effective atomic number, K1 and K2 constants, and A is the atomic mass. The exponent is heuristically found to be n ∼ 4. The attenuation coefficient defined this way can fit experimentally measured data with good precision using the method of least square fits. Instead of mathematical descriptions, one can use the linear attenuation curves of two natural materials with two significant benefits. The first one is the increased accuracy of physical descriptions. Namely, it has been shown by authors following Alvarez's work that photoelectric dependency on n ∼ 4 does not reach sufficient accuracy in the energy range from 30 to 140 keV for CT applications. This is because the energy dependence of coefficient n cannot be neglected. Secondly, the mathematical description of the photoelectric effect and Compton scattering creates two basis vectors that span the space where all possible materials can be found. The choice of two material basis vectors enlarges the narrow part of this space. One could necessarily think of this transformation as a magnification of the area of interest in the space of all possible materials. Every material that has higher photoelectric or Compton absorption of chosen basis materials is characterized by negative value in this space. Materials that were bundled together from the perspective of theoretical "complete PE-CE basis" can be distinguished better and seen as separate materials.

In this work, three different sets of basis materials were examined – water and adipose (WA), polyethylene and Teflon (polytetrafluoroethylene; PP) as well as PMMA and aluminum (PA). Critical evaluation based on different matrices leads to the choice of PA as the best fit. The most crucial parameter is taken to be a separation between phantom materials in the basis material histogram (see **Fig. 18**). Another important characteristic to be considered was the level of spread (i.e., implied uncertainty) onto the original positions of found materials within the histogram. The terms position uncertainty and basis material histogram will become clear in the following description. In the PA basis, PMMA describes well Compton scattering while there is a high occurrence of the photoelectric effect in aluminum for the applied energy range. The research done on the conventional dual-energy unit showed the fitting error increases when the density of generic material is similar to the density of chosen basis materials. Also, the goodness of the fitting procedure is increased for more considerable differences in the composition of basis materials and generic material [29].

Because of the reason already mentioned, the transition from (35) to real attenuation curves of chosen materials was performed. The two materials, PMMA and Al, are labeled as 1 and 2. Their linear

attenuation coefficient strictly depends on effective atomic numbers Z_1 and Z_2, densities and the atomic masses A_1 and A_2. For the sake of simplicity, in this theoretical derivation, the atomic mass will be roughly approximated to $A \sim 2\,Z$. This is true for elements of interest composting organic tissues, such as carbon, nitrogen, oxygen, etc.

$$\mu_i(\rho_i, Z_i, 2Z_i); i = 1,2 \tag{37}$$

By applying the above definition to each basis material, and then solving the equation (35) in terms of f_{PE} and f_{CE}, one obtains an expression of the attenuation coefficient of a generic material in terms of the attention coefficients of the basis as

$$\mu = \frac{\rho \left(\mu_1 + \frac{(-Z^n Z_1 + Z Z_1^n) Z_2 (-\mu_2 \rho_1 + \mu_1 \rho_2)}{Z(-Z_1^n Z_2 + Z_1 Z_2^n)\rho_2} \right)}{\rho_1} \tag{38}$$

Dependence has been fully moved to a combination of functions μ_1 and μ_2, while coefficients associated with them are the coordinates of the material with respect to the basis materials. Values n, ρ_1, ρ_2, Z_1, and Z_2 are known and for the chosen basis are 4, 1.19, 6.56, 2.7, and 13, respectively.

Decomposing the equation (38) in terms of μ_1 and μ_2, extracted coefficients are respectively

$$x_1 = \frac{Z^n Z_1 Z_2 \rho - Z Z_1 Z_2^n \rho}{Z Z_1^n Z_2 \rho_1 - Z Z_1 Z_2^n \rho_1} \tag{39}$$

$$x_2 = \frac{Z^n Z_1 Z_2 \rho - Z Z_1^n Z_2 \rho}{Z Z_1^n Z_2 \rho_2 - Z Z_1 Z_2^n \rho_2} \tag{40}$$

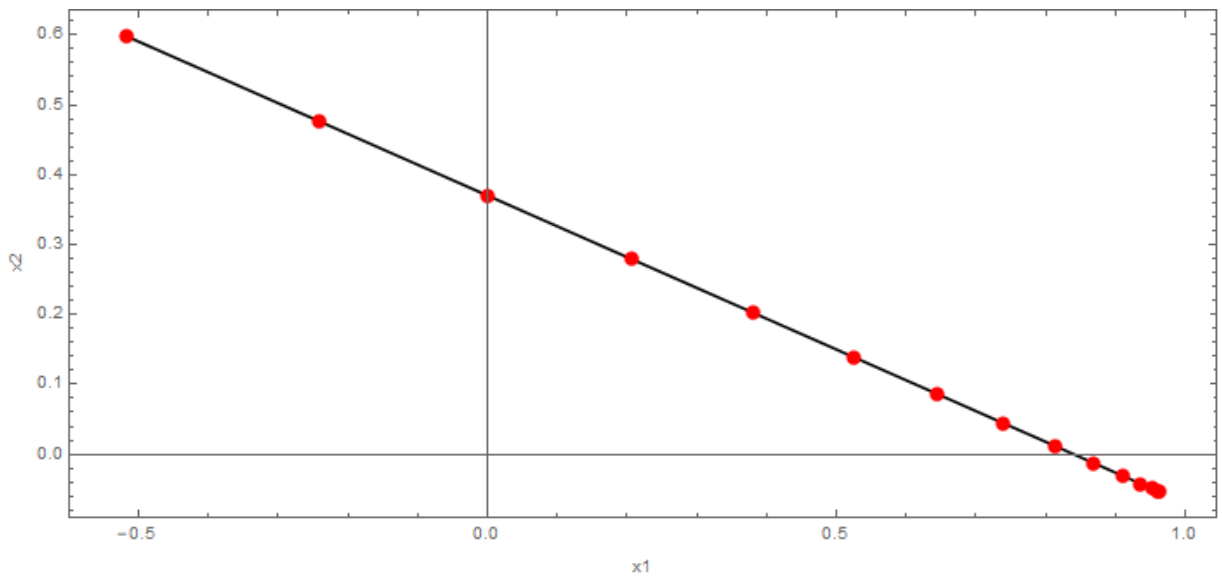Keeping ρ fixed and varying Z, the coordinates draw up along a straight line shown in **Fig. 9**.

Fig. 9 Straight line along which Z values are increased from Z=1 to Z=15; at the same time density was kept constant

A linear equation defines the straight line as

$$x_2(x_1) = \alpha x_1 + \beta \tag{41}$$

Considering that $x_2(0) = \rho/\rho2$ and $x_2(\rho/\rho1)=0$, coefficients α and β can be found and equation rewritten as

$$x_2 = \frac{\rho - x_1\rho_1}{\rho_2} \tag{42}$$

A consequence of the above remarks is that there is one direction in the plane that only depends on the material density ρ. That is the direction orthogonal to the straight line, while the dependence on Z is uniquely mapped onto the direction parallel to the straight line. The knowledge of the line angular coefficient α allows the definition of a suitable rotation matrix. Applying the matrix of the form

$$\begin{bmatrix} \dfrac{\rho_1}{\sqrt{1 + \dfrac{\rho_1^2}{\rho_2^2}}\rho_2} & \dfrac{1}{\sqrt{1 + \dfrac{\rho_1^2}{\rho_2^2}}} \\[4ex] \dfrac{-1}{\sqrt{1 + \dfrac{\rho_1^2}{\rho_2^2}}} & \dfrac{\rho_1}{\sqrt{1 + \dfrac{\rho_1^2}{\rho_2^2}}\rho_2} \end{bmatrix} \tag{43}$$

rotates the original coordinates resulting in the following expression for the rotated coordinates

$$x_1 = \frac{\rho}{\sqrt{1 + \dfrac{\rho_1^2}{\rho_2^2}}\rho_2} \tag{44}$$

$$x_2 = \frac{\rho\left(Z^n Z_1 Z_2 (\rho_1^2 + \rho_2^2)\right) - Z(Z_1^n Z_2 \rho_1^2 + Z_1 Z_2^n \rho_2^2)}{Z(-Z_1^n Z_2 + Z_1 Z_2^n)\rho_1 \sqrt{1 + \dfrac{\rho_1^2}{\rho_2^2}}\rho_2^2} \tag{45}$$

Fig. 10 shows this dependence. Different points along each line represent varying effective atomic numbers Z for materials of interest. As already mentioned, density is mapped on lines parallel to each other in the orthogonal direction.
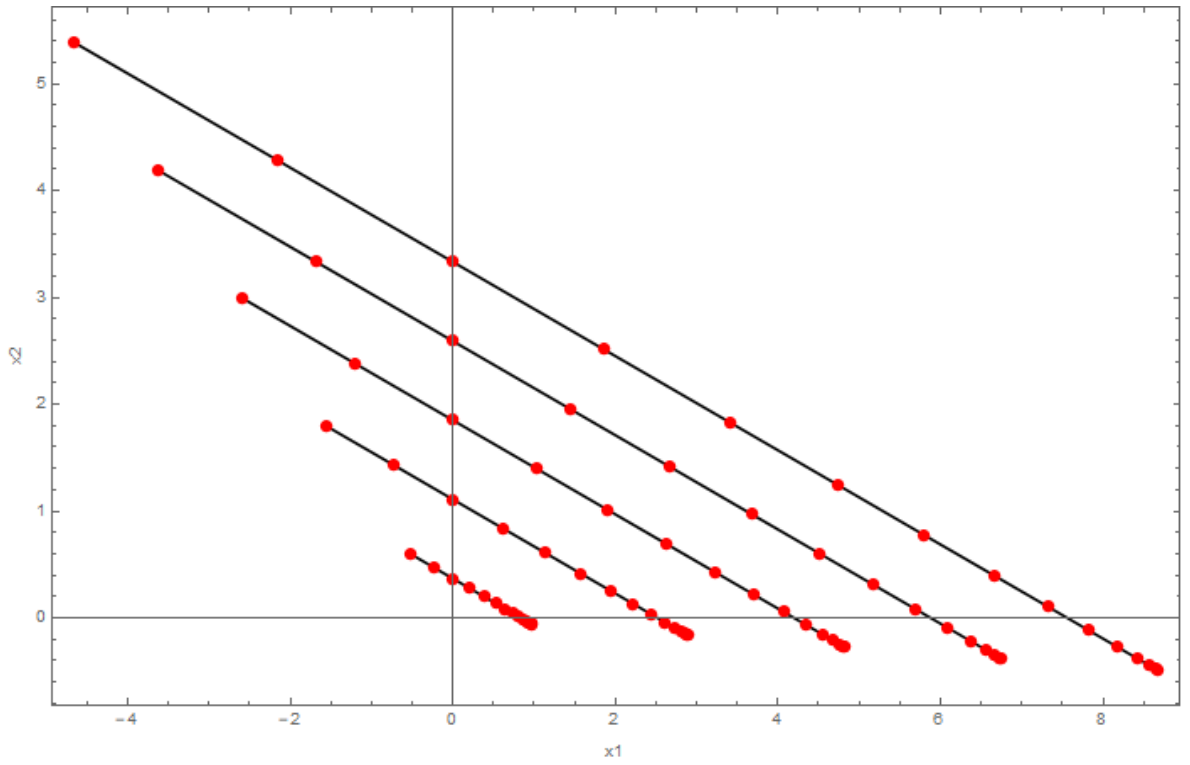
Fig. 10 The graph very similar to the previous one. Lines parallel to each other are created as a result of varying the density values along with Z. Density is increased starting from the lower-left corner and grows for lines moving toward the upper right corner of the graph.

The ρ dependence can be removed from the second rotated coordinate by dividing it by the first one. This finally leads to a fully decoupled set of coordinates given in the equations   (46) and   (47).

$$x_\rho = \frac{\rho}{\sqrt{1 + \frac{\rho_1^2}{\rho_2^2}}\,\rho_2} \tag{46}$$

$$x_Z = -\rho_2^2 + \frac{\dfrac{(-Z^n Z_1 + Z Z_1^n)Z_2(\rho_1^2 + \rho_2^2)}{Z(Z_1^n Z_2 - Z_1 Z_2^n)}}{\rho_1 \rho_2} \tag{47}$$

The visual confirmation that the coordinate transformation decouples ρ and Z dependences is shown on the final **Fig. 11**. The transition from **Fig. 10** to **Fig. 11** reflects the transition from equations (44) and   (45) to the equations   (46) and   (47).
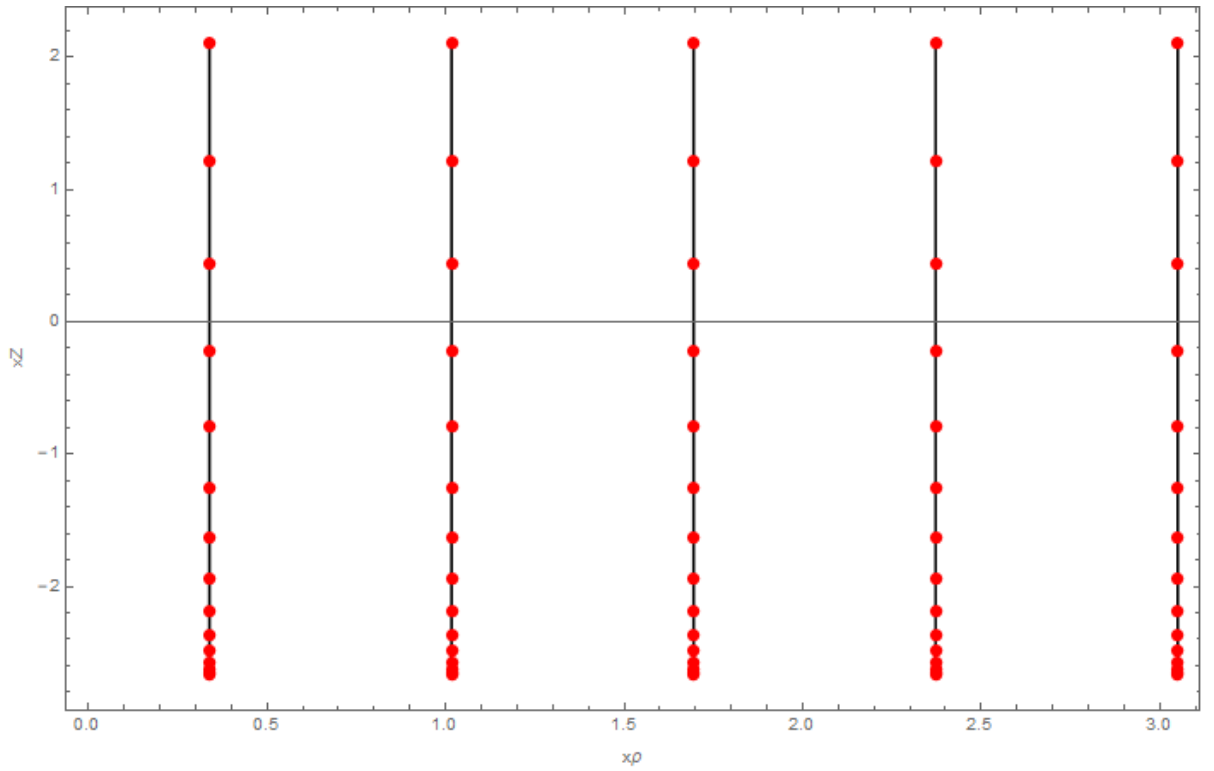
Fig. 11 After described transformations, effective atomic number and density quantities are independently observed

In this decoupled coordinate frame, the xZ coordinate acquires the handy dependence given as

$$xZ(Z) = pZ^{n-1} + q \tag{48}$$

while xρ coordinate is linearly dependent on the density

$$x\rho(\rho) = r\rho + s \tag{49}$$

2.2 Phantom

The custom-made phantom dedicated to calibration and quality control of the SYRMA-3D imaging chain was used in this investigation. It is a round shape cylinder made of PMMA and filled with demineralized water. The water inside the phantom provides a uniform layer useful for the measurement of the uniformity of CT reconstruction and evaluation of reconstruction artifacts. Inside of it, six different inserts were placed. These cubic rods are made of 5 different materials labeled in **Fig. 12**. Materials are polyethylene (PE), nylon (PA), polymethyl methacrylate (PMMA), polyoxymethylene (POM), and polytetrafluoroethylene (PTFE). The attenuation curves of these materials are given below.

Fig. 12 Linear attenuation coefficients of phantom inserts

The choice of materials was made to mimic different tissues found inside the breast. The attenuation curves of all the plastic materials composing the phantom were accessed via the database [20].

Fig. 13 Schematic representation of the in-house made SYRMEP phantom used for image acquisition

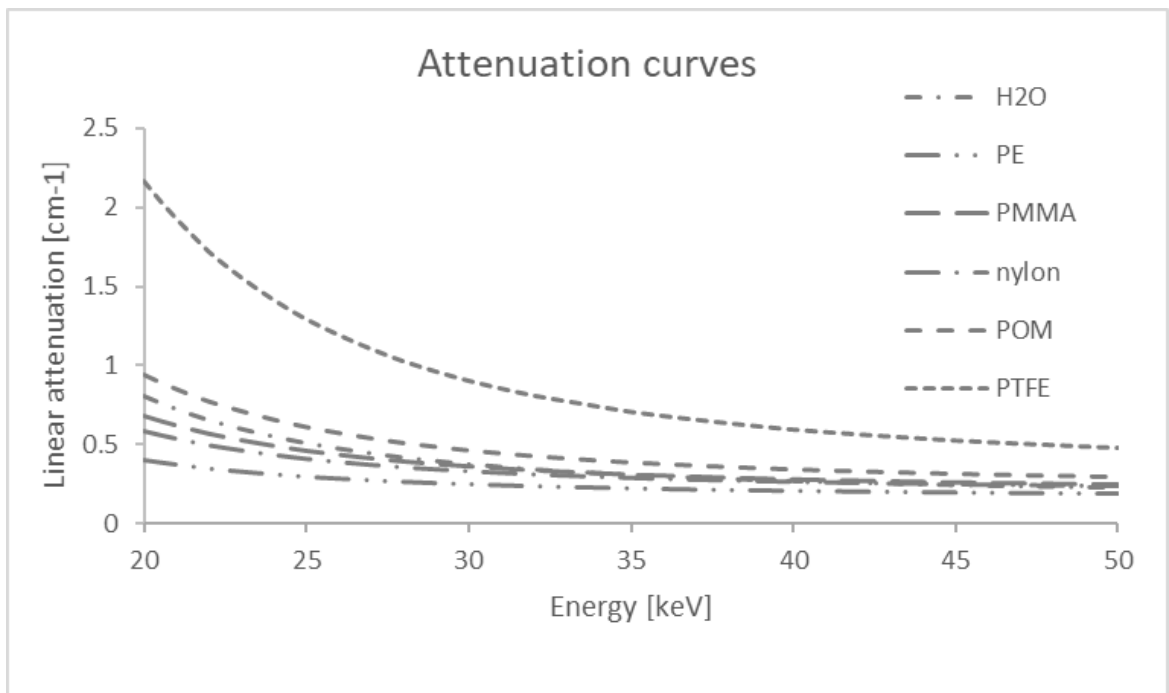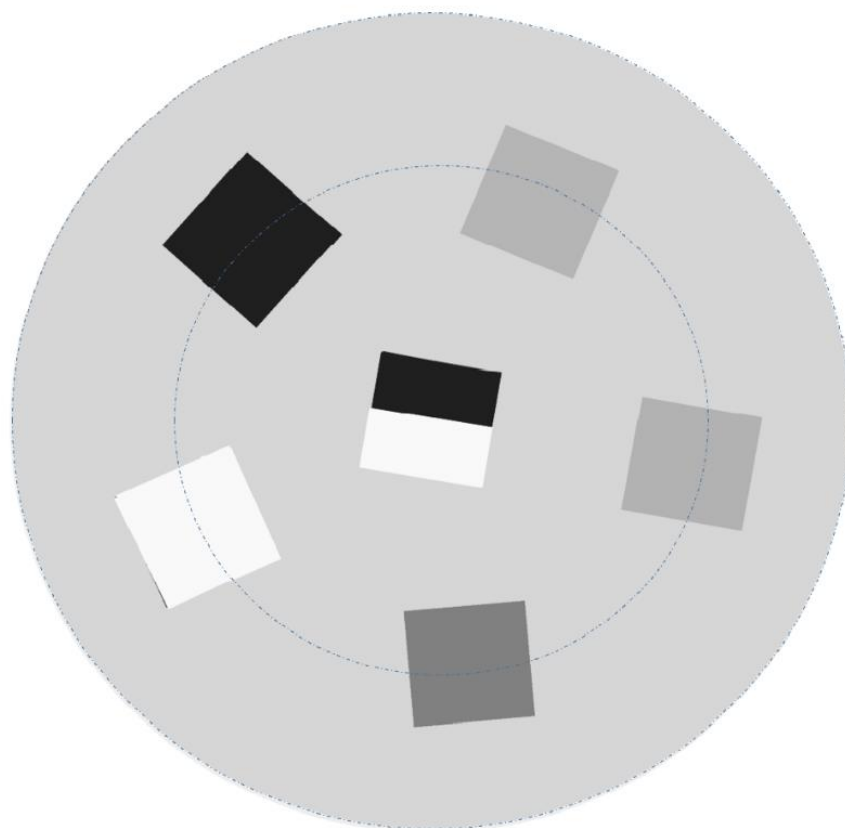**Fig. 13** is a schematic view of the phantom with all of its inserts with each shade of gray representing a certain type of material. The outer radius of the circular phantom is 10 cm and the inner circle, at which perimeter plastic inserts are arranged, has a radius of 8 cm. The phantom is intended to serve as a tool for performing a regular quality control measurement in which CT number linearity and accuracy of reconstructed attenuation coefficients will be assessed. It is also used for the measurement of spatial uniformity and noise fluctuation in the water as well as the accuracy of the attenuation coefficient for water [29]. For the purpose of this work, the phantom is used as a tool for calibration of effective atomic number and density values. It is possible because these values are known a priori for all the materials comprising the phantom.

Table 1 Phantom materials with corresponding chemical formula, Z_{eff} and density

Material	Water	PE	PA	PMMA	POM	PTFE
Chemical formula	H_2O	$(C_2H_4)_n$	$(C_{12}H_{22}N_2O_2)_n$	$(C_5O_2H_8)_n$	$(CH_{20})_n$	$(C_2F_4)_n$
Effective atomic number	7.51	5.53	6.21	6.56	7.03	8.48
Density [g cm^{-3}]	1	0.93	1.14	1.19	1.42	2.25

2.3 Data acquisition

Phantom images were acquired at the SYRMEP beamline at the Italian synchrotron facility in Trieste. The distinct features of the experimental setup are synchrotron source and propagation-based imaging method. Once interacting with the breast phantom content, the beam continues to propagate freely for 3.7 meters until reaching the detector. During this time, the significant part of scattered radiation has traveled away from the detector allowing for the elimination of anti-scatter grids. A total of 66 slices were acquired for four distinct beam energies of 25, 28, 32, and 35 keV. These values are selected with a resolution of 0.1 % using two Si (1,1,1) crystal monochromators. The beam surface is of rectangular shape with 220 mm in horizontal and 4 mm in the vertical direction. Its main properties are laminar shape, high fluence, and monochromaticity of great energy resolution. Given these attributes, the SYRMEP beamline effectively exploits the phase-contrast imaging method previously mentioned. It allows for significant improvement of image quality, maintaining the reference dose levels in mammography. Once phase information is acquired by the detector, the mathematical method in the opposite direction is applied to track back to the source of the phase shift and recover attenuation values. Striped to its essence, this method cleverly utilizes the fact that noise is not carried by the beam but rather formed on the detector. When going in the opposite direction, mathematical convolution decreases the random noise contribution. Signal-to-noise gain (SNR_g) between non-propagated and propagated images was studied within the SYRMEP project by Brombal et al. [30]. In this work maximum of $SNR_g = 20$ was experimentally observed for a distance of 6.4 meters, which is a great improvement but still 2 times lower than theoretical predictions. It is also true that at the same time, the resolution which was increased during free-space propagation is now deteriorated to its original values leaving it practically unaltered. After phase-retrieval, images are reconstructed through filter back projection with Shepp-Logan filtering. The source of radiation is distant and of small dimensions but fixed in space. Therefore, the patient support table had to be specially designed with two degrees of freedom – movement in upward-downward direction and rotation. Projections are typically acquired over 180 degrees with a rotation speed of 4.5 deg s^{-1}.

Fig. 14 The rotating treatment table

The final product is 66 slices at 4 energy values, cleaned from most imaging artifacts, and co-registered so that pixel position of neighboring slices corresponds to the same spatial position in the horizontal direction. Slices of each energy have been calibrated to obtain quantitative linear attenuation coefficient maps. First, regions of interest were selected, and average gray levels measured. Calibration is performed with respect to theoretical linear attenuation coefficients of phantom materials at given energies. Straight calibration lines, together with their equations, are given in **Fig. 15**.
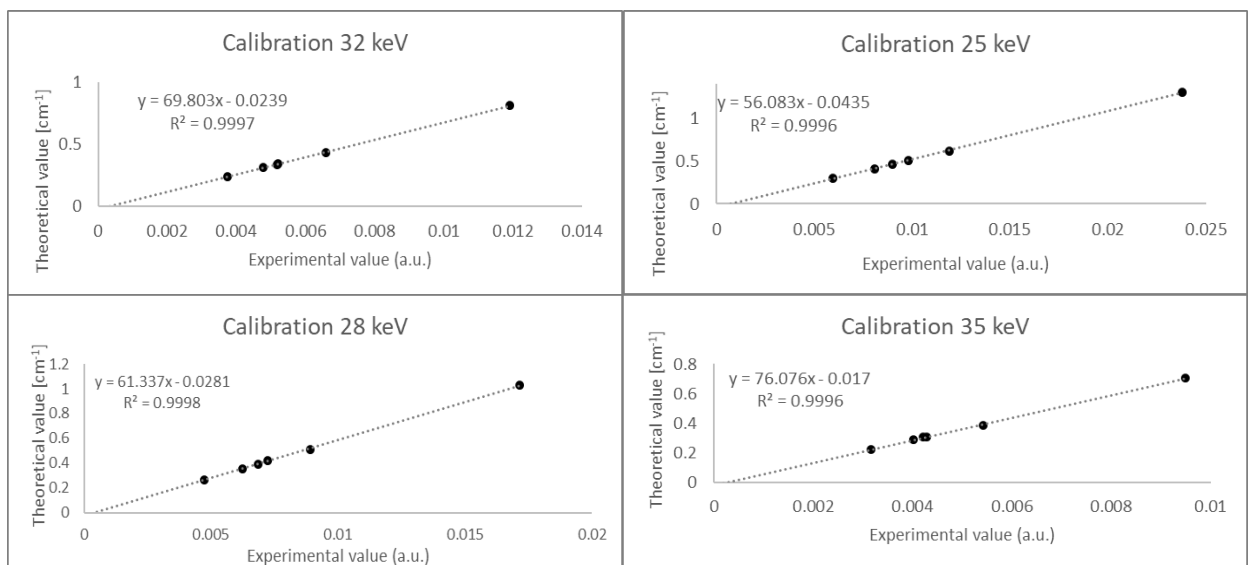

Fig. 15 Calibration curves relating experimental data to the a priori known linear attenuation coefficients of phantom materials

Calibrated images served as an input for theoretical manipulation described in the previous chapter. Contillo et al. performed an analysis on this topic, referring to the accuracy of the reconstructed attenuation coefficients of the plastic materials through linearity assessment [29].

2.4 Estimation of the mean glandular dose

To describe the absorbed dose to the breast, in mammography mean glandular dose (MGD) is estimated. The incident air kerma is measured on the surface of the breast. The relation between air kerma and MGD is dependent on the glandularity and thickness of the breast. The proportional term is estimated through Monte Carlo simulations, run in GEANT 4 code by Longo et al. [31]. It is of importance to stress that another existing quantity, the total mean glandular dose MGD_t, defines the ratio of total energy deposited to the whole breast and the glandular mass within this volume. Therefore, MGD converges to total MGD as the irradiated volume approaches the size of the whole breast. In the case of this experiment, the total mean glandular dose for the phantom images was set to be 20 mGy. To put in perspective, the American College of Radiology (ACR) protocol recommends that this value for an ACR accrediting phantom shall not exceed 3 mGy. Although this substantial difference in dose delivered is often not tolerated from the radiological point of view, it was needed for initial testing of this method. At this stage of our project, images of real breast samples are acquired at doses of 5 mGy, which is more than two times lower compared to conventional BCTs. With the expected upgrade of the beamline, precisely by increased object-to-detector distance, it is estimated that this dose will be pushed down to the 2 mGy while preserving the same image quality [33]. This ultimately leads to mean glandular doses comparable to the digital mammography values.

3   Research results and their discussion

In this chapter, the result of each stage of the process will be presented. At this point, we have calibrated images of the phantom at 4 energies. They are graphically shown in the form of the stack in **Fig. 16** A. Using the theoretical description of linear attenuation coefficients for PMMA and Al, images are transformed in the two basis images using the recipe previously presented.
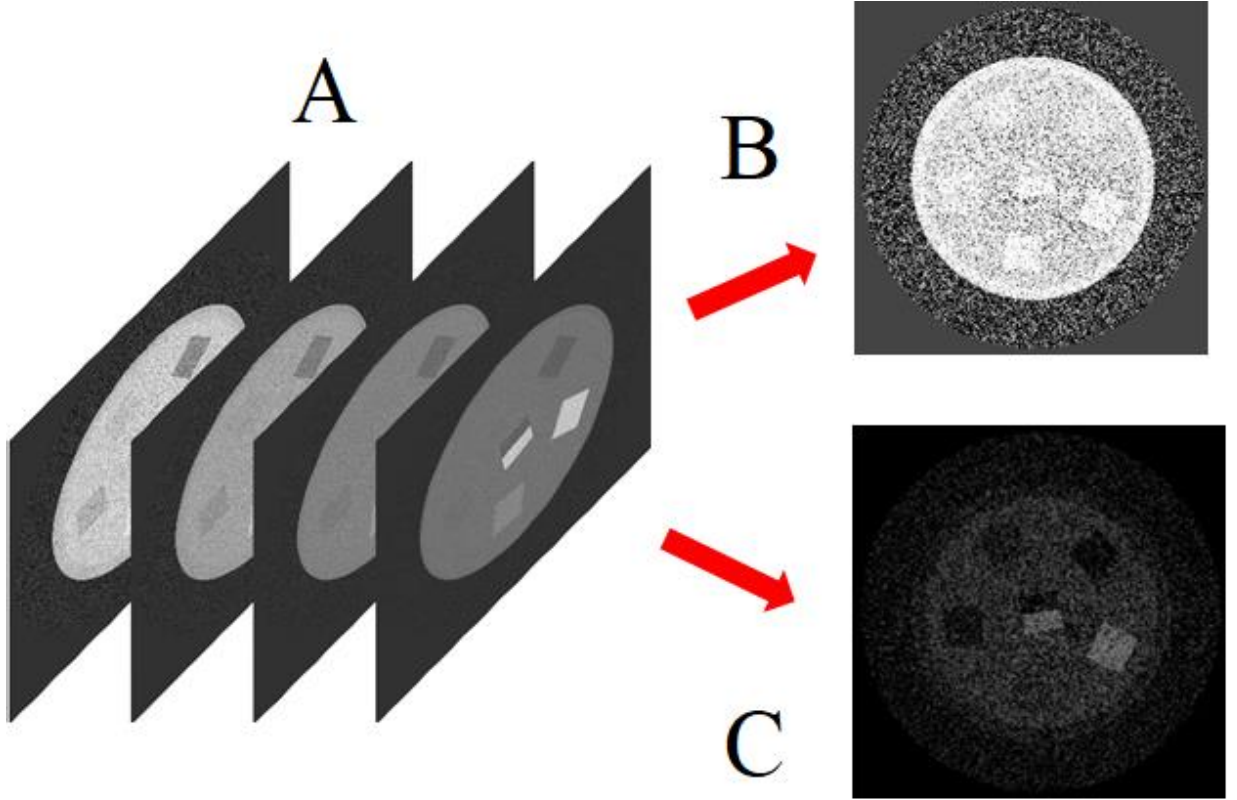

Fig. 16 A. Aims to show the stack of 4 images of the same phantom position but at different energies. When images are well co-registered, every spatial position corresponds to the right pixel in all four images. The 4 pixels at the same position are then fitted with equation   (34) to be represented as some combination of PMMA linear attenuation coefficient (picture B) and Al attenuation coefficient (picture C).

One can think of the graph above as a visual representation of the material decomposition for the attenuation curves of the phantom inserts shown previously in **Fig. 12**. The fact that we have images at 4 energies practically increases the goodness of fit. Products are two matrices of x_1 and x_2 coefficients (also called weights), which, when represented in grayscale values, give two separate images.

$$\mu(E) = x_1 \, \mu_{PMMA}(E) + x_2 \, \mu_{Al}(E) \qquad (50)$$

The benefit of spectral decomposition can already be seen at this point. Some inserts easily visible in the aluminum-basis image are not that obvious in the PMMA-based image and vice versa. However, to continue with our goal of quantitative description, each of the product images was flattened into a vector. Pixels with zero value, which corresponds to the attenuation of the air, were filtered out, while all the other were appended to vectors. These two vectors were then used to construct a histogram with PMMA-based image values lined up in the horizontal and Al-based image values lined up in the orthogonal direction. In the plain of the histogram, points should appear at coordinates x_1 and x_2, whose combination most accurately describes the attenuation of present materials. Since in our

phantom, there are 5 different materials surrounded by water – 6 distinct points are "expected." The air around the phantom is automatically removed with a geometrical cut. Coordinates of theoretically described materials are shown in **Fig. 17**.
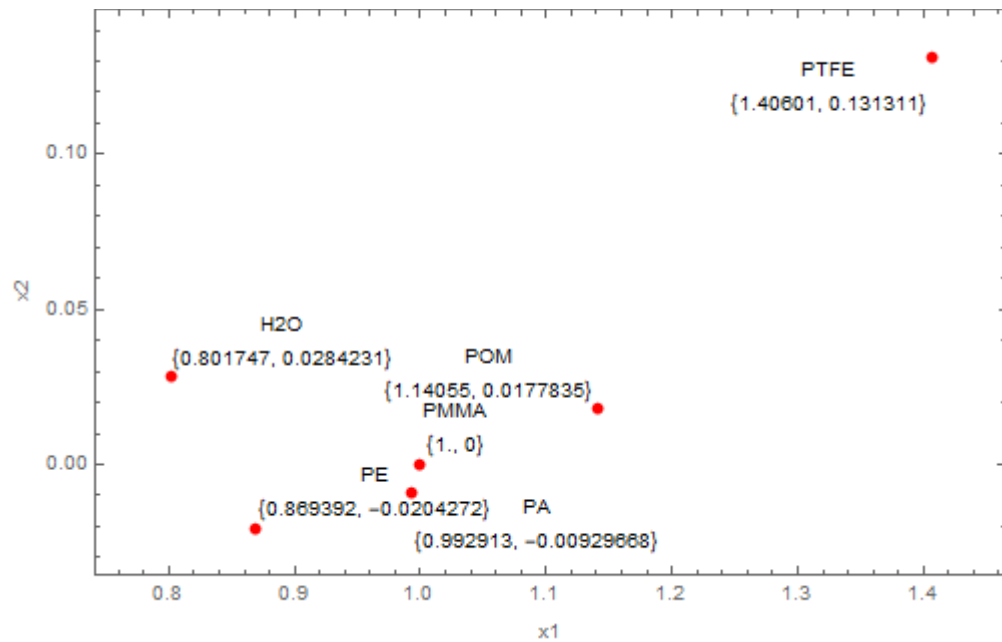

Fig. 17 Theoretically predicted materials position in the histogram, before any transformation applied

The insert made of PMMA has it's position precisely at coordinates (1,0), which is to be expected since the x-axis is made up of weights for PMMA's attenuation curve, against the y-axis made of weights for aluminum's attenuation curve and has value 0. The equation (50) for PMMA material simply reduces to the

$$\mu_{PMMA}(E) = x_1 \, \mu_{PMMA}(E) \qquad (51)$$

where x_1 is exactly 1. All the other materials in the graph are described as some ratio of the basis material weights. The third dimension in the theoretical graph is a sharp peak with its height limited by the amount of the material present in the image. Although theoretical derivation yields beautifully separated points representing each material with sharp peaks, in practice, it is not exactly the case. Due to the presence of noise and limited detector resolution, grey levels corresponding to pixels of the same material slightly differ, causing the spread of points into the "bubbles". Influence on their spread has the co-registering technique of the system; pixel positions at 4 different energy images must remain the same. Since incrementing of one coefficient typically implies the decrement of the other, these bubbles are elongated from the south-west to the north-east direction. The peak intensity information is available in the form of a luminance map. Phantom images in this experiment were of the size 2839 x 2839 pixels. Created PMMA and Al basis images are, therefore, of the same size. This vast number of pixels flattened in two vectors is used to create a 2D histogram. The brightest bins in the histogram contain the highest number of pixels, and as this number is going down, the bins become less visible. The highest portion of SYRMEP phantom is water, creating a strong bubble partially obscuring and overlapping with bubbles coming from other materials. The binning size of the histogram is 400 x 400 in both directions and red dots correspond to theoretical values previously shown in **Fig. 17**.
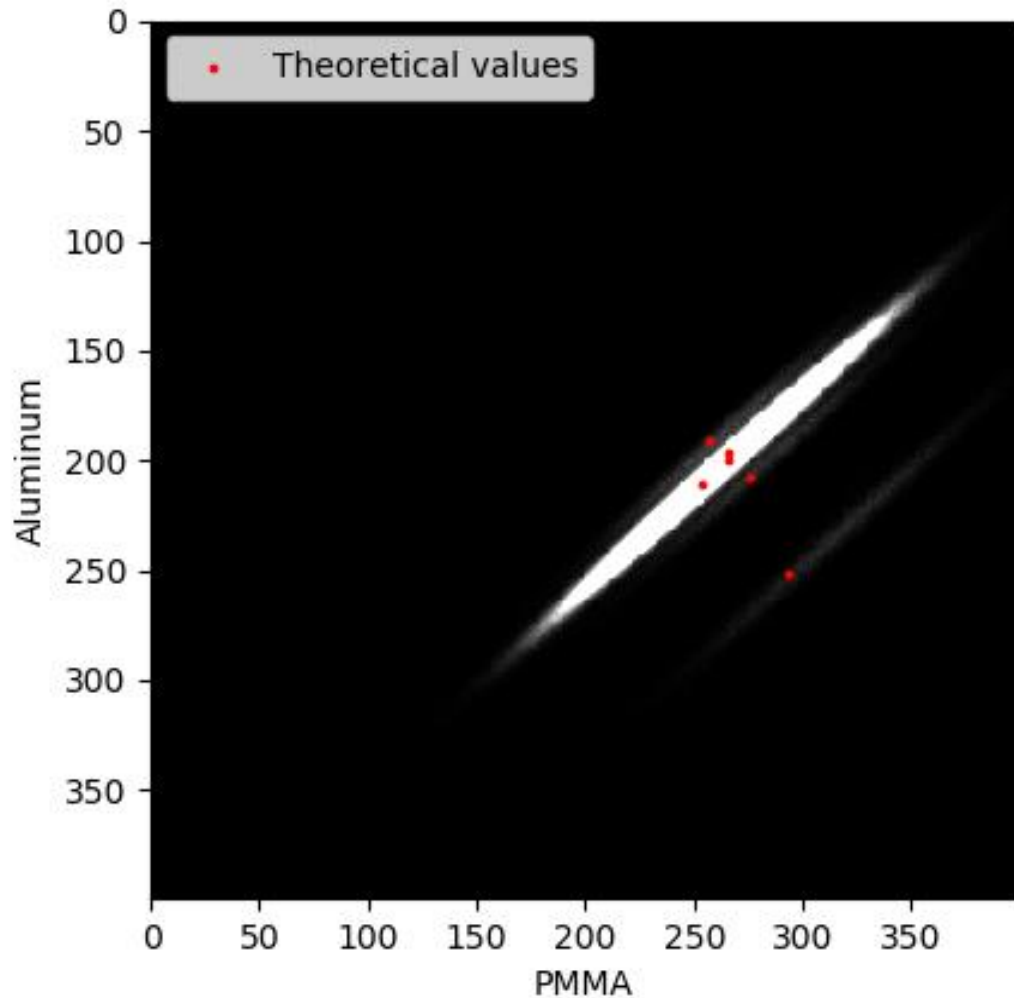
Fig. 18 The 2D histogram containing the ellipsoids created by the presence of various materials in the phantom image. The horizontal axis contains all the pixel values of PMMA image flattened into the vector and vertical axis consists of flattened Al image. Pixels having nearly the same ratio of μ(PMMA) and μ(Al) contributions will populate the same bin in the histogram. How much this ratio could differ until pixel is assigned to adjacent bin is determined by the binning size of the histogram. Red dots superimposed on the histogram represent ideal theoretical material positions.

These elongated "mountains" with its peaks around theoretical values are then fitted with 2D Gaussian curves. The game of adjusting the resolution of the histogram by changing the number of bins (or the size of the histogram) has proven to be valuable for better fitting of the data. In the experiment, the amount of specific material present in the image can be estimated by calculating the integral under the Gaussian curve. This is closely related to the spread of the 2D Gaussian curve in the two orthogonal directions and its height. Retrieved parameters of 6 Gaussian fitting procedure leave us with the experimental positions.

Table 2 Theoretical and experimental positions of phantom materials within the histogram **Fig. 18**

Material	x_{theory}	y_{theory}	x	y
H20	0.802	0.028	0.797	0.027
PE	0.869	-0.020	0.856	-0.019
PA	0.993	-0.009	0.994	-0.009
PMMA	1.000	0.000	1.000	0.000
POM	1.141	0.018	1.136	0.019
PTFE	1.406	0.131	1.378	0.127

Although some bubbles in the histogram are heavily overlapped, forming the bright one in the middle of the histogram created system managed to distinguish between them with great accuracy, which will be assessed later. In **Table 2**, x and y theory refers to the theoretical values of the center of the bubble, while x and y are the centroids of the fitted Gaussians. For the sake of comparing the theoretical and experimental positions x and y, the scatter plot (**Fig. 19**) is given.
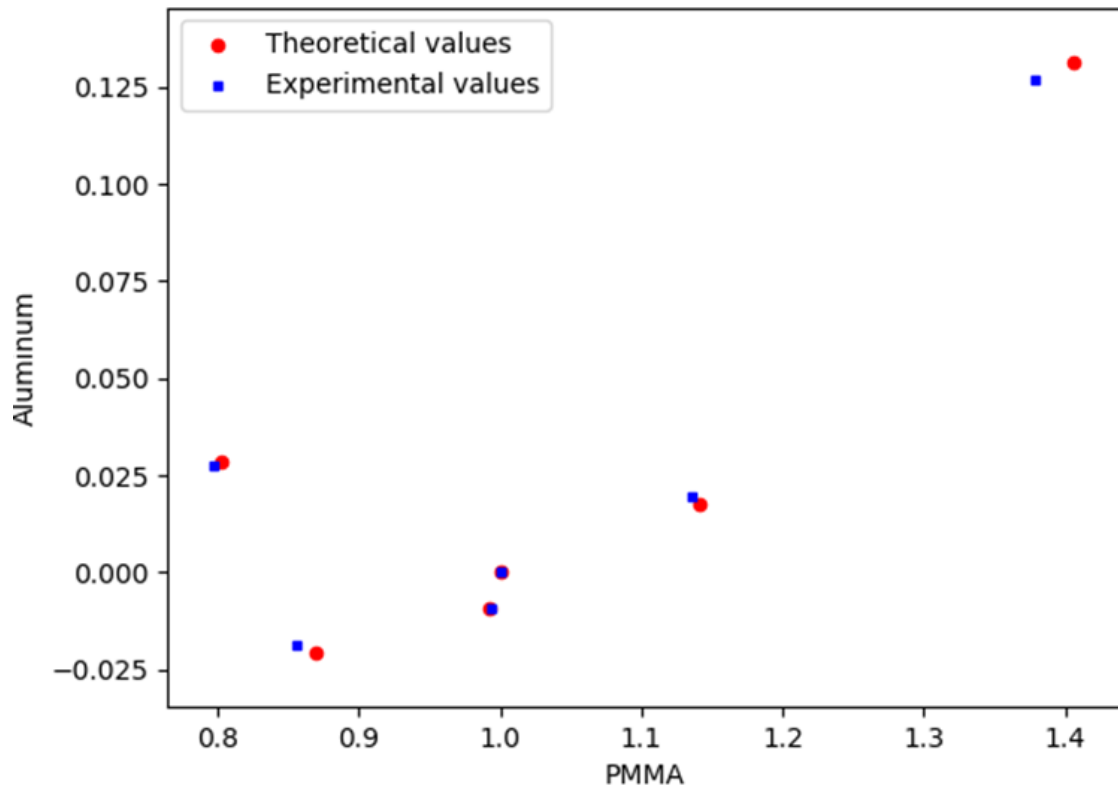
Fig. 19 Theoretical and experimental position comparison.

It is worth taking a moment to emphasize the importance of the obtained results plotted in the graph above. The fact that the system was able to find local maximums and successfully fit Gaussians to presented data allowed for the straightforward application of the developed theory. Other parameters estimated by the fitting routine are peak intensity, the maximum counts at (x,y) positions. The σ_u and σ_v are the spreads of the Gaussians in orthogonal directions.

Table 3 Maximum intensity values, spread in major and minor ellipsoid axis, and the angle θ between the major axis and horizontal axis of the histogram

Material	Peak intensity	σ_u	σ_v	θ
H20	1710	4.33E-01	7.44E-03	-0.123
PE	1292	3.29E-01	7.49E-05	-0.135
PA	832	7.64E-01	9.90E-05	-0.116
PMMA	1540	3.37E-01	4.70E-05	-0.116
POM	66	4.65E-01	8.17E-03	-0.123
PTFE	53	6.08E-01	1.03E-02	-0.124

Subscripts u and v refer to the major and minor axis of the ellipse that is being fitted. The difference of a few orders of magnitude between the σ_u and σ_v follows the visual impression shown in **Fig. 18**. The slope at which bubbles are preferably spread is at the almost constant angle $\theta \sim -0.12$. After applying a suitable rotation matrix (equation (43)) to experimental values, centroid values move to the new positions. The next step follows the transformation described by equation (47), ultimately leading to a decoupled atomic number and density dependence of each material. These values are shown in the graph below.
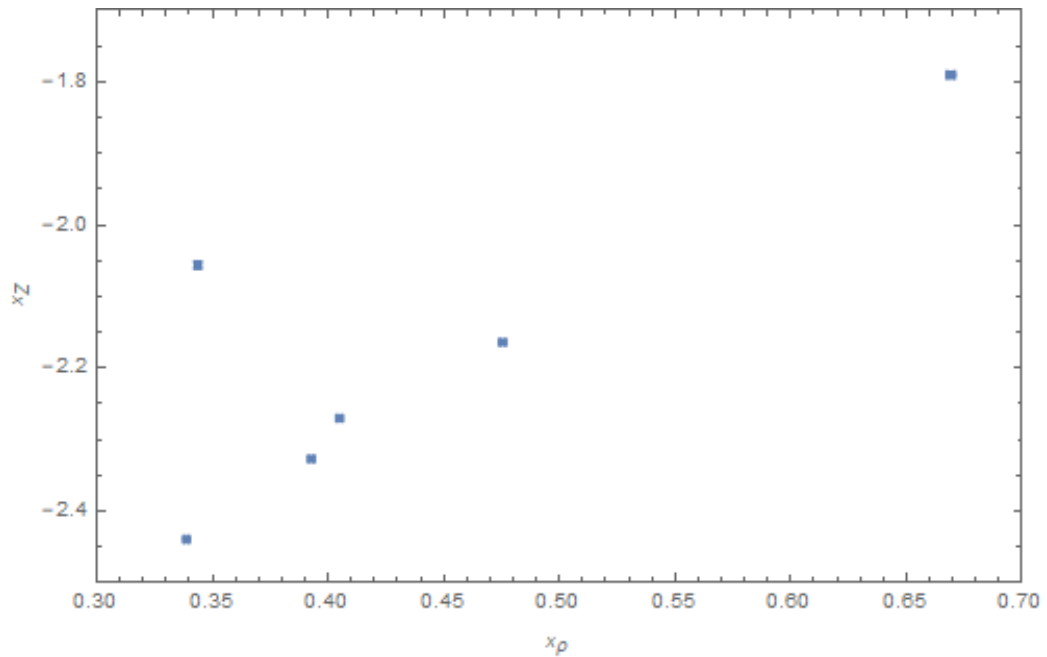
Fig. 20 Positions in the new reference frame (the result of rotation and subsequent division x2/x1) with the corresponding propagated standard error values in both directions

Fig. 20 is an experimental analog of the final **Fig. 11** presented in theoretical derivation. Data points exhibit error bars that are very small and, therefore, difficult to distinguish. Yet, these are not final quantitative values for Z_{eff} and density, but they had to be calibrated against the known values for phantom materials.

3.1 Calibration procedure

To determine the quantitative relationship between Z_{eff} and x_Z, a nonlinear optimization was applied to achieve a least-squares fit of all data points to the function form in equation (48). Fitting the equation (48) to these points, and therefore the estimation of parameters p and q, ultimately lead to the formation of the calibration curve, which can be later used to calculate unknown Z_{eff} values from a real breast sample. The parameters of the polynomial fit are p = 0.0005787 and q = -2.6013502. Additionally, instead of being a constant parameter, n can also be estimated with the same fitting procedure. In this case, it is slightly above 4 (estimated n = 4.26), which yields a better fitting curve. Listed values on the ordinate of **Fig. 21** spanning the range of atomic numbers from 5.5 to 8.5 are of the interest for most of the breast tissues, including the effective atomic numbers of various soft tissues. The success of the fitting method demonstrates that Z_{eff} can be quantitatively determined using a simple power function with the addition of a constant of the same form suggested by the theory (see equation (48)).
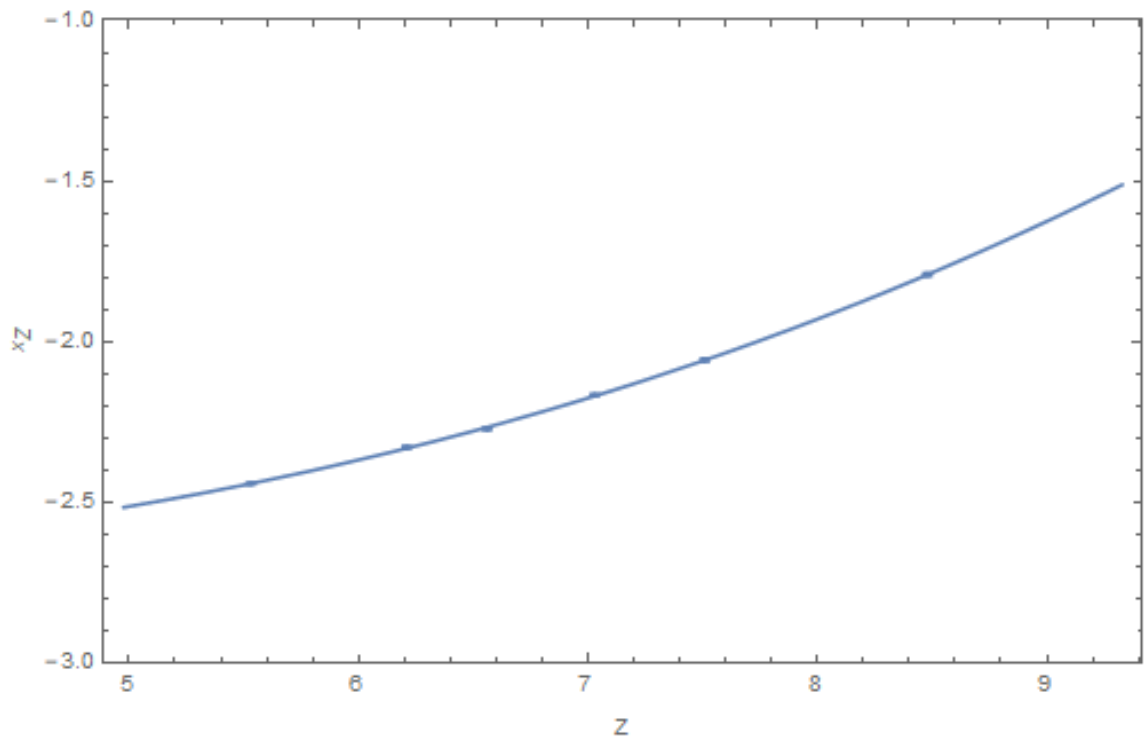

Fig. 21 Calibration curve 1- measured data x_Z against a priori known effective atomic numbers Z

On the other hand, the simple linear dependence of x_ρ versus ρ is shown in **Fig. 22**.
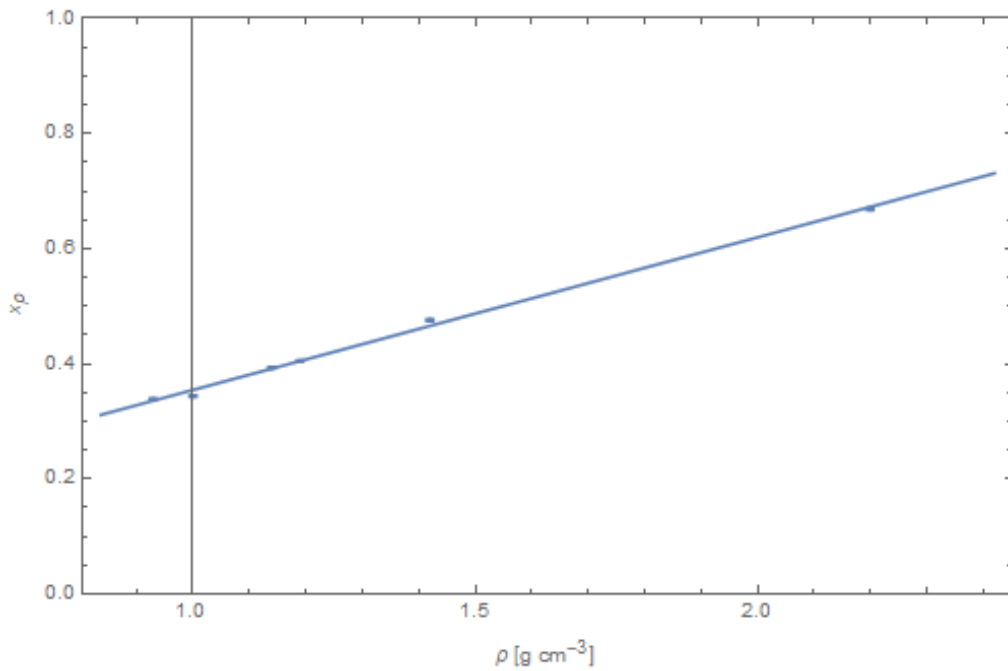
Fig. 22 Calibration curve 2 - measured data x_ρ against a priori known densities ρ

In analogy with the previous method, a priori known densities of phantom materials were used for the construction of the density calibration curve. Here, the parameters of the fitted line are r = 3.8321 and s = -0.3509, and the correlation coefficient between the experimental and known density values is 0.996. This demonstrates the quantitative accuracy of spectral decomposition in the measurement of material density. Linear dependence leads to a straightforward solution for estimating the density of an unknown tissue in the sample. Finally, two calibration curves allow very accurate access to decoupled information of density and effective atomic number of each sample present in a phantom.

Fig. 23 The final data for effective atomic number and density together with standard error bars

3.2 Propagation of measurement uncertainties

The fit procedure individuates a preferred direction, identified by the angle θ, aligned to the major axis (u) of the ellipse that is being fitted. The two widths σ_u and $\sigma_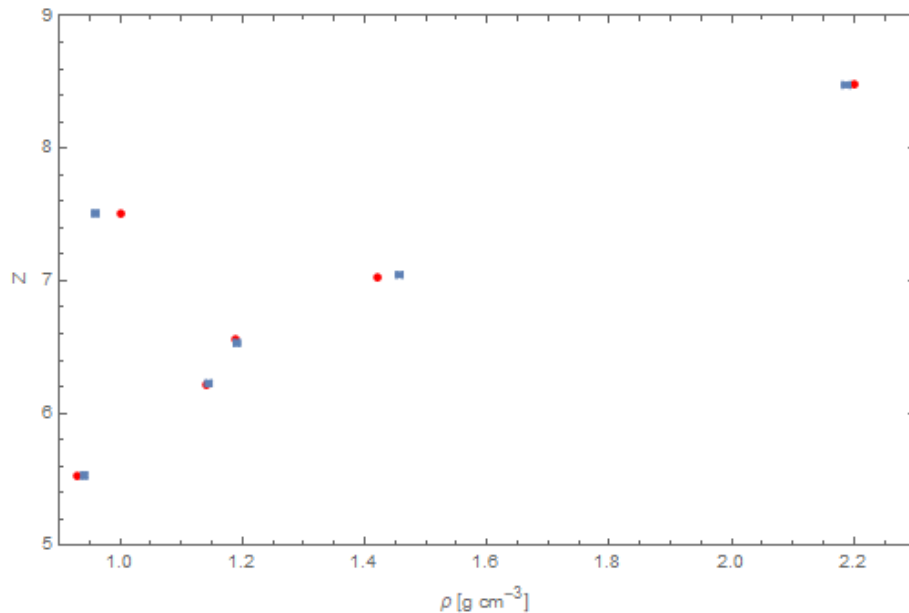v$ are then identified as the standard deviations associated with the measured position in a reference frame $\{x_u, x_v\}$ whose coordinates are completely uncorrelated (see Appendix 1). The total volume V under each Gaussian in bins can be calculated using peak intensity A and widths σ_u and σ_v information available as an output of the fitting process.

$$V = 2\pi\, A\, \frac{\sigma_u\, \sigma_v}{p_x\, p_y} \tag{52}$$

Entities p_x and p_y are pixel sizes in the horizontal and vertical direction. The standard error is obtained by dividing standard deviations σ_u and σ_v by the square root of the volume under corresponding 2D Gaussian. This is true under the assumption that the volume under each Gaussian is equal to the total number of pixels contributing to the corresponding 2D Gaussian function.

$$\sigma_{su} = \sigma_u \big/ \sqrt{V} \;\; ; \;\; \sigma_{sv} = \sigma_v \big/ \sqrt{V} \tag{53}$$

The aim is to translate these standard errors into uncertainties of the coordinates in a rotated frame identified by the angle $\varphi = \arctan(\rho_2/\rho_1)$, whose coordinates are labeled $\{x_1, x_2\}$. For the PA basis, angle $\varphi = 1.15567$. From this rotated frame, the uncertainties must be propagated to the rescaled frame $\{x_\rho, x_Z\}$ and from there finally to the pair $\{\rho, Z\}$.

First, we rotate the frame. When rotating from a frame identified by an angle θ to another frame identified by an angle φ, the rotation matrix is

$$\begin{pmatrix} x_1 \\ x_2 \end{pmatrix} = \begin{bmatrix} \cos\alpha & \sin\alpha \\ -\sin\alpha & \cos\alpha \end{bmatrix} \begin{pmatrix} x_u \\ x_v \end{pmatrix} \tag{54}$$

where $\alpha = \varphi - \theta$. The law of propagation of uncertainties states that, for a function ω of n variables t_i, the variance of ω reads

$$\sigma_\omega^2 = \sum_{i=1}^{n} \left(\frac{d\omega}{dt_i}\right)^2 \sigma_{t_i}^2 \tag{55}$$

which in the case of the equation (55) gives

$$\sigma_{x_1}^2 = \sin^2\alpha\, \sigma_{su}^2 + \cos^2\alpha\, \sigma_{sv}^2 \tag{56}$$

$$\sigma_{x_2}^2 = \cos^2\alpha\, \sigma_{su}^2 + \sin^2\alpha\, \sigma_{sv}^2 \tag{57}$$

After the rotation, comes the rescaling of the second coordinate. Since $x_\rho = x_1$, propagating the x_ρ uncertainty is trivial

$$\sigma_{x_\rho} = \sigma_{x_1} \tag{58}$$

while the rescaling of $x_Z = x_2 / x_1$ implies that

$$\sigma_{x_Z}^2 = \frac{x_2^2}{x_1^4}\sigma_{x_1}^2 + \frac{1}{x_1^2}\sigma_{x_2}^2 \tag{59}$$

Finally, the propagation to the pair $\{\rho, Z\}$. Once again, since $x_\rho = \kappa\,\rho$, the propagation is trivial

$$\sigma_\rho = \kappa^{-1}\sigma_{x_\rho} \tag{60}$$

While the more complicated relationship $x_Z = p\,Z^{n-1} + q$ gives

$$\sigma_Z = \frac{\lambda\,(x_Z - q)^{\lambda-1}}{p^\lambda}\sigma_{x_Z} \tag{61}$$

Where $\lambda = 1\,/\,n - 1$. Propagated uncertainties are shown in the previous graphs in the form of uncertainty bars on the experimental results. Here, the original values are presented.

Table 4 Experimental values for density and effective atomic number together with propagated standard errors

$\rho \pm \sigma_\rho$ [g cm^{-3}]	$Z \pm \sigma_Z$
0.934 ± 0.004	5.53 ± 0.02
1.194 ± 0.004	6.53 ± 0.01
1.146 ± 0.004	6.22 ± 0.01
1.471 ± 0.005	7.04 ± 0.01
2.232 ± 0.006	8.48 ± 0.01
0.953 ± 0.004	7.51 ± 0.02

3.3 Discussion

The effective atomic number for phantom materials mimicking a soft tissue is scattered in the region of about ± 15 % around the average value of 6.57. This indicates that their separation is more obvious comparing their effective atomic numbers rather than their composition values. The same conclusion was drawn by M. Thorikoshi et al. [24] in a very similar study using the synchrotron source dual-energy imaging. Their aim was extracting electron density information with application to error estimation for proton and heavy-ion radiotherapy. The precision of obtained information is comparable with the results presented in this thesis, except the fact that in this work, actual values for mass density were presented. Other similar work with the same goal of extracting electron density and effective atomic number based on phase-contrast CT imaging was performed by Zhihua Qi et al. [16]. The calibration curves for both quantitative values are of the same form. However, the PTFE material could not be successfully fitted to the linear dependence of calibrated versus reference electron density. In this thesis, all data points, including PTFE, were fitted to a linear function, which might be thanks to the absence of beam hardening effects due to the monochromatic source of radiation. The effective atomic numbers for the water, PMMA and POM are in an excellent agreement across mentioned studies, as well as to the theoretical ground-truth values. The comparison of the three same materials used in phantom studies is given in Table 5.

Table 5 Inter-study comparison of material effective atomic numbers

Material	Water	PMMA	POM
Chemical formula	H_2O	$(C_5O_2H_8)_n$	$(CH_{20})_n$
Theoretical values	7.51	6.56	7.03
Zhihua Qi et al.	7.42	6.47	6.95
M. Thorikoshi et al.	7.39	-	-
Present work	7.51	6.53	7.04

The major limitation of using synchrotron source radiation in the purpose of breast tumor diagnosis is its high cost to benefit ratio. The technology applied is sophisticated and synchrotron facilities usually do not provide a clinical environment. Still, the studies [33,36] performed to compare the image quality of synchrotron radiation and conventional BCT found that high signal to noise ratio in phase-sensitive imaging offers a clear advantage in soft imaging. Alternatives to providing monochromatic sources with high enough flux for the purpose of breast imaging are already in the stage of development [34]. Nonetheless, high-quality images served as an initial stage of the model development. Formally, it can be applied to any other multi-energetic stack of well co-registered images.

Conclusion

1. The images used are superior to images produced in conventional CT unit in terms of SNR and CNR.

2. The proposed method is capable of obtaining effective atomic number and density information with the precision of more than one percent. It concludes that the variations of the effective atomic number and density are sufficiently small to be interpreted as the characteristic constant for a material.

3. The theoretical model of high accuracy was developed. The assumptions made during the derivation of the model do not affect the outcome of calculations significantly. Moreover, the theoretically predicted calibration functions were successfully fitted to the experimental data with high accuracy.

4. Therefore, the proposed model gives outstanding results for the characterization of similar low-Z materials contained inside the breast. Based on evidence gathered on phantom images, the method could be applied to the detection of tumorous tissue inside the real breast samples.

The efforts in the future will be put toward testing this method on the mastectomy samples obtained after surgical procedure. After histological examination, samples would be imaged with the same experimental setup. The developed model will be applied with the aim of characterizing malignant tissue in terms of effective atomic number and composition. Such a procedure has the potential of detecting tumorous masses at an early stage while it still doesn't grow to the sizes that become visible in the image. More importantly, the characterization of the chemical composition of developed tissue could be of help for the determination of its potential malignancy.

Acknowledgments

List of references

[1] FERLAY, Jacques, et al. Estimating the global cancer incidence and mortality in 2018: GLOBOCAN sources and methods. *International journal of cancer*, 2019, 144.8: 1941-1953.

[2] CRONIN, Kathleen A., et al. Annual Report to the Nation on the Status of Cancer, part I: National cancer statistics. Cancer, 2018, 124.13: 2785-2800.

[3] YIP, Cheng-Har. Breast cancer in Asia. In: Cancer Epidemiology. *Humana Press*, 2009. p. 51-64.

[4] YAFFE, Martin J. Mammographic density. Measurement of mammographic density. *Breast Cancer Research*, 2008, 10.3: 209.

[5] HENRIKSEN, Emilie L., et al. The efficacy of using computer-aided detection (CAD) for detection of breast cancer in mammography screening: a systematic review. *Acta Radiologica*, 2019, 60.1: 13-18

[6] KATZEN, Janine; DODELZON, Katerina. A review of computer aided detection in mammography. *Clinical imaging*, 2018, 52: 305-309.

[7] ERHARD, Klaus, et al. Characterization of cystic lesions by spectral mammography: results of a clinical pilot study. *Investigative radiology*, 2016, 51.5: 340-347.

[8] I. source, "AB-CT—Advanced Breast-CT GmbH," www.ab-ct.com/, Erlangen, Germany, Accessed: 15 April 2019.

[9] I. source, "Koning breast CT," http://koninghealth.com/en/kbct, West Henrietta, NY, Accessed:15 April 2020.

[10] MURPHY, Lesley M. Linear feature detection and enhancement in noisy images via the Radon transform. *Pattern recognition letters*, 1986, 4.4: 279-284.

[11] D. J. P. Ehsan Samei, Hendee ' s physics of medical imaging, fifth edition, New Jersey : JohnWiley & Sons, Inc., 2019.

[12] BROMBAL, Luca, et al. Large-area single-photon-counting CdTe detector for synchrotron radiation computed tomography: a dedicated pre-processing procedure. *Journal of synchrotron radiation*, 2018, 25.4: 1068-1077.

[13] PAGANIN, David, et al. Simultaneous phase and amplitude extraction from a single defocused image of a homogeneous object. *Journal of microscopy*, 2002, 206.1: 33-40.

[14] CONTILLO, Adriano; TAIBI, Angelo. Material characterisation in phase contrast imaging: The basis decomposition method revisited. *EPL (Europhysics Letters)*, 2017, 117.4: 48003.

[15] NUGENT, K. A., et al. Quantitative phase imaging using hard x rays. *Physical review letters*, 1996, 77.14: 2961.

[16] QI, Zhihua, et al. Quantitative imaging of electron density and effective atomic number using phase contrast CT. *Physics in Medicine & Biology*, 2010, 55.9: 2669.

[17] BRAIG, Eva, et al. Direct quantitative material decomposition employing grating-based X-ray phase-contrast CT. *Scientific reports*, 2018, 8.1: 1-10.

[18] PIAI, Anna, et al. Quantitative characterization of breast tissues with dedicated CT imaging. *Physics in Medicine & Biology*, 2019, 64.15: 155011.

[19] GUREYEV, Timur E., et al. On the "unreasonable" effectiveness of transport of intensity imaging and optical deconvolution. *JOSA A*, 2017, 34.12: 2251-2260.

[20] PRONYAEV, V. G. *XMuDat: Photon attenuation data on PC. Version 1.0. 1 of August 1998. Summary documentation*. International Atomic Energy Agency, 1998.

[21] ALVAREZ, Robert E.; MACOVSKI, Albert. Energy-selective reconstructions in x-ray computerised tomography. *Physics in Medicine & Biology*, 1976, 21.5: 733.

[22] LEHMANN, L. A., et al. Generalized image combinations in dual KVP digital radiography. *Medical physics*, 1981, 8.5: 659-667.

[23] MCCOLLOUGH, Cynthia H., et al. Dual-and multi-energy CT: principles, technical approaches, and clinical applications. *Radiology*, 2015, 276.3: 637-653.

[24] TORIKOSHI, Masami, et al. Electron density measurement with dual-energy x-ray CT using synchrotron radiation. *Physics in Medicine & Biology*, 2003, 48.5: 673.

[25] FREDENBERG, Erik, et al. Measurement of breast-tissue x-ray attenuation by spectral mammography: solid lesions. *Physics in Medicine & Biology*, 2016, 61.7: 2595.

[26] FREDENBERG, Erik, et al. Measurement of breast-tissue x-ray attenuation by spectral imaging: fresh and fixed normal and malignant tissue. *Physics in Medicine & Biology*, 2018, 63.23: 235003.

[27] D. D. R. W. .. e. a. Fredenberg E., "Measurement of breast-tissue x-ray attenuation by spectral mammography: first results on cyst fluid," *Physics in Medicine & Biology,* vol. 58, no. 24, 2013.

[28] FREDENBERG, Erik, et al. Measurement of breast-tissue x-ray attenuation by spectral mammography: first results on cyst fluid. *Physics in Medicine & Biology*, 2013, 58.24: 8609.

[29] CONTILLO, Adriano, et al. A proposal for a quality control protocol in breast CT with synchrotron radiation. *Radiology and oncology*, 2018, 52.3: 329-336.

[30] BROMBAL, Luca, et al. Monochromatic breast computed tomography with synchrotron radiation: phase-contrast and phase-retrieved image comparison and full-volume reconstruction. *Journal of Medical Imaging*, 2018, 6.3: 031402.

[31] LONGO, Renata, et al. Advancements towards the implementation of clinical phase-contrast breast computed tomography at Elettra. *Journal of synchrotron radiation*, 2019, 26.4.

[32] BROMBAL, LUCA. X-ray Phase-Contrast Tomography: Underlying Physics and Developments for Breast Imaging. 2020.

[33] BROMBAL, Luca, et al. Image quality comparison between a phase-contrast synchrotron radiation breast CT and a clinical breast CT: a phantom based study. *Scientific reports*, 2019, 9.1: 1-12.

[34] BROMBAL, L., et al. Monochromatic propagation-based phase-contrast microscale computed-tomography system with a rotating-anode source. *Physical Review Applied*, 2019, 11.3: 034004.

[35] LONGO, Renata, et al. Clinical study in phase-contrast mammography: image-quality analysis. *Philosophical Transactions of the Royal Society A: Mathematical, Physical and Engineering Sciences*, 2014, 372.2010: 20130025.

[36] BROMBAL, Luca, et al. Phase-contrast breast CT: the effect of propagation distance. *Physics in Medicine & Biology*, 2018, 63.24: 24NT03.

Appendices

Appendix 1. The correlation of Gaussian fit parameters

The 2D histogram in **Fig. 18** shows the presence of 4 distinct data spreads in the form of an ellipsoid, while 2 more are expected to be obscured by the brightest bubble caused by the water in the phantom. This is because PMMA and PA materials have similar linear attenuation coefficients to the water attenuation coefficient and this translates to similar spatial positions in the 2D histogram. In addition, since most of the phantom is water, its presence in the histogram is superior and manifested as a very bright area obscuring other materials with very similar properties. The expected blurring of otherwise theoretically precise positions in the histogram is mostly due to created image noise during detector measurement. A noise source of stochastic nature is typically well described by a Gaussian kernel, whose width represents the typical random spread of the original signal. Besides, material ellipsoids have preferred orientation at the angle θ of about - 0.12 radians between its major axis and horizontal axis of the histogram. Therefore, the 2D histogram data was fitted with a priori defined 2D Gaussian function g(x,y) with the same orientation.

$$g(x, y) = A\, e^{-\left(\frac{(x\,\cos\theta + y\,\sin\theta)^2}{2\,\sigma_{su}^2} + \frac{(y\,\cos\theta - x\,\sin\theta)^2}{2\,\sigma_{sv}^2}\right)} \tag{62}$$

The notation is consistent with the previously presented equations and the outcome of scipy.optimize.curve_fit method within Python 3.0 language was presented in **Table 3**. Later, in the chapter assessing the propagation of the measurement uncertainty, it was claimed that coordinates in a reference frame $\{x_u, x_v\}$ are totally uncorrelated. The reference frame $\{x_u, x_v\}$ has a x_u axis which coincides with the direction of the major axis of histogram ellipsoids and the σ_u spread of fitted 2D Gaussian. The x_v axis coincides with the direction of the minor axis and the σ_v spread of the same Gaussian. In other words, there is no angular correlation between coordinates since θ is 0. Deviations σ_u and σ_v given as an estimation parameter of the applied fitting method belong to the 2D Gaussians in the form:

$$g'(x_u, x_v) = A'\, e^{-\left(\frac{x_u^2}{2\,\sigma_u^2} + \frac{x_v^2}{2\,\sigma_v^2}\right)} = A'\, e^{-\frac{x_u^2}{2\,\sigma_u^2}}\, e^{-\frac{x_v^2}{2\,\sigma_v^2}} \tag{63}$$

In this form, we have a product of the two Gaussians with totally uncorrelated distributions.